REVIEW

ADVANCED MATERIALS TECHNOLOGIES

www.advmattechnol.de

In Situ and Operando Analyses of Reaction Mechanisms in Vanadium Oxides for Li-, Na-, Zn-, and Mg-Ions Batteries

Sul Ki Park, Wesley M. Dose, Buddha Deka Boruah, and Michael De Volder*

Due to their diversity in the composition, lattice structures and physical/chemical properties, and various oxidation states (2+, 3+, 4+, and 5+), (V_xO_y) nanomaterials have attached much attention for developing new rechargeable batteries, including lithium-ion batteries (LIBs), sodium-ion batteries (NIBs), zinc-ion batteries (ZIBs), and magnesium-ion batteries (MIBs) as well as new energy storage concepts such as light-rechargeable batteries. However, to further improve the electrochemical performance of V_xO_y-based batteries, it is crucial to understand the various electrochemical mechanisms taking place in these materials for LIBs, NIBs, ZIBs, and MIBs. This review covers a systematical discussion of in situ and operando analysis methods carried out on V_2O_5, VO_2, $Li_xV_yO_z$, $Na_xV_yO_z$, $Zn_xV_yO_z$, and $Mg_xV_yO_z$ for LIBs, NIBs, ZIBs, and MIBs and the fundamental insights they have provided in the energy storage mechanisms in these batteries.

1. Introduction

To cope with our society's continued high energy consumption and push toward renewable energy, there is a demand for electrochemical energy storage devices with enhanced capacity.[1–3] Lithium-ion batteries (LIBs) are at the forefront of high energy and power density applications needed in electric vehicles and sodium-ion (Na^+), zinc-ion (Zn^{2+}), and magnesium-ion (Mg^{2+}) chemistries are promising for large-scale storage of energy harnessed from renewable energy sources.[4–9]

The active electrode materials used in battery electrodes have a direct impact on the electrochemical performance including the capacity, energy and power density, cycling stability, safety, and cost. Vanadium oxide (V_xO_y) nanomaterials have attracted increasing attention for rechargeable batteries because of its crystal structure and electrochemical properties.[10–13] The compositions, lattice structures, and physical properties vary depending on the oxidation state of vanadium, and as a result, different forms of vanadium oxide show different electrochemical performance and storage mechanisms (**Table 1**).[10–13] The diversity in crystal structures of V_xO_y provides opportunities to use these materials for LIBs, sodium-ion batteries (NIBs), zinc-ion batteries (ZIBs), and magnesium-ion batteries (MIBs).[13–15]

In particular, V_2O_5 and VO_2(B) have been investigated intensively as electrode materials in LIBs.[11,12,15–20] Their large open channels and tunnels allow for intercalation/de-intercalation of other ions such as Na^+, Zn^{2+}, and Mg^{2+}.[11,12,15–20] However, the electrochemical storage mechanism of these ions is different because of changes in the ionic radius (0.76, 1.02, 0.74, and 0.72 Å for Li^+, Na^+, Zn^{2+}, and Mg^{2+}, respectively) and electrostatic interaction with multivalent ions.[13,21–25]

Nevertheless, commercial applications of V_xO_y cathodes are still limited primarily because the material is synthesized in its charged state (i.e., without a source of intercalation ions: Li, Na, Zn, and Mg) and the toxicity. To address the former, chemical insertion of ion sources into the V_xO_y host materials has been studied, including Li_x–, Na_x–, Zn_x–, and Mg_x–V_yO_z.[24–30] The intercalated ions not only act as pillars into the interlayer to prevent structural deformation, but also increase the amount of ion sources in the layer.

Previous review papers comprehensively reported the characterization of V_xO_y-based materials and summarized their electrochemical performance for application as cathodes in LIBs, NIBs, ZIBs, and MIBs.[12,13,25,26] However, it is essential to understand the energy storage mechanisms in detail, for which in situ/operando techniques are attractive because they monitor the real-time reactions during charge and discharge. Here, "in situ" refers to "on site or inside the reactant" whereas "operando" refers to "under working or operating conditions," however these terms are often used interchangeably in literature. More generally, "in situ/operando analysis" is used to describe electrochemical analysis under real-time electrochemical operation.[31–34]

This review provides a systematic overview of the state-of-the art progress in in situ/operando analysis of V_xO_y materials for LIBs, NIBs, ZIBs, and MIB, with major results and mechanistic discussion for effective in situ/operando techniques that will assist in developing promising high-performance vanadium oxide-based energy storage systems (**Figure 1**). We

---

S. K. Park, W. M. Dose, B. D. Boruah, M. De Volder
Department of Engineering
University of Cambridge
Cambridge CB3 0FS, UK
E-mail: sp991@cam.ac.uk
W. M. Dose
Department of Chemistry
University of Cambridge
Lensfield Road, Cambridge CB2 1EW, UK

The ORCID identification number(s) for the author(s) of this article can be found under https://doi.org/10.1002/admt.202100799.

DOI: 10.1002/admt.202100799

Table 1. The properties of vanadium oxides such oxidation states and lattice system.[10–13]

Oxidation states of V	V^{2+}	V^{3+}	V^{4+}	V^{5+}
Chemical formula	VO	V_2O_4	VO_2	V_2O_5
Lattice system	Octahedral	Trigonal	Monoclinic	Orthorhombic

will first discuss X-ray diffraction (XRD) analysis, followed by X-ray absorption near edge structure (XANES) and extended X-ray absorption fine structure (EXAFS), Raman, combination of optical characterization and UV-Vis, transmission electron microscopy (TEM), and finally atomic force microscopy (AFM).

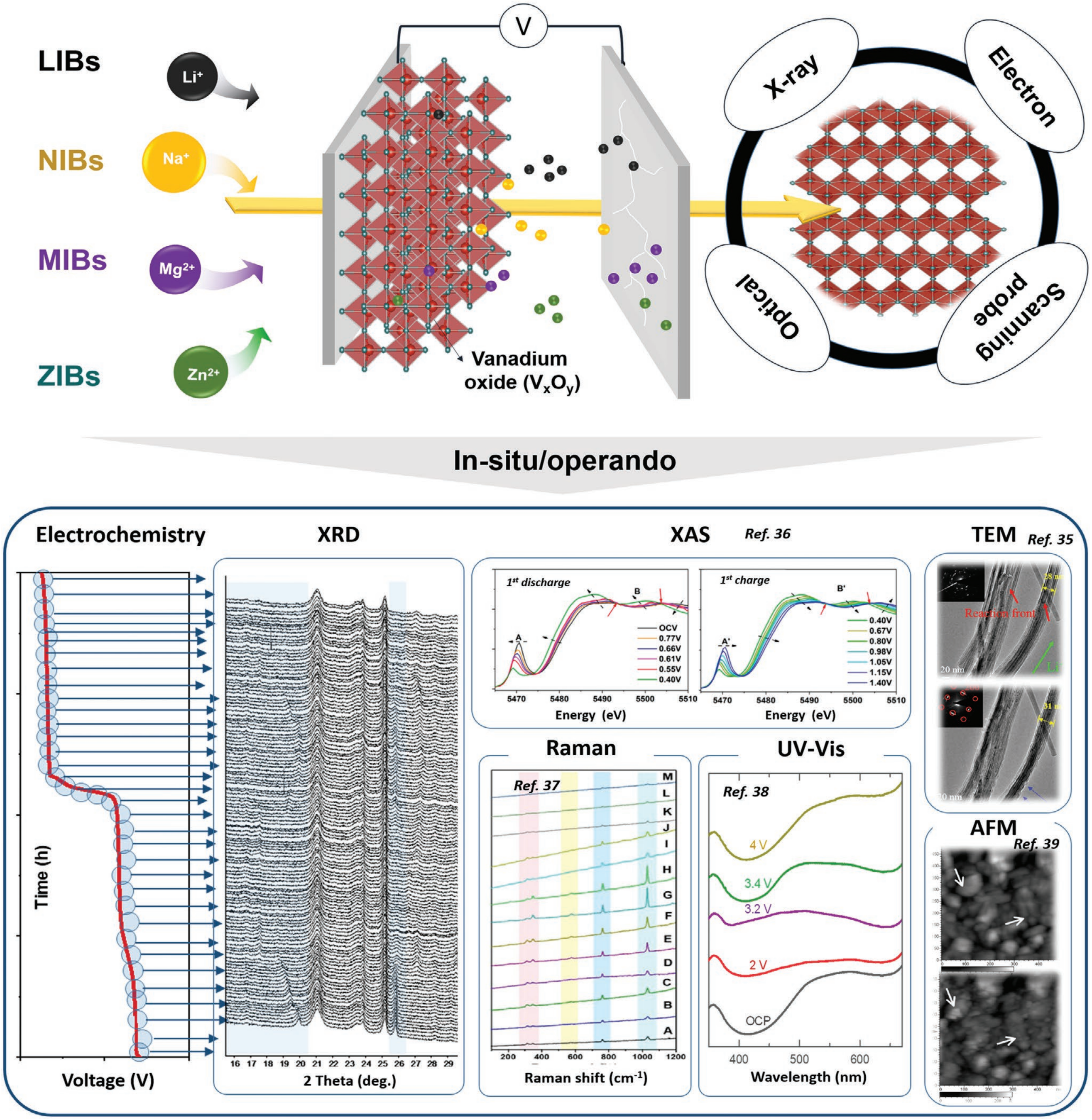

Figure 1. Schematic of Li-, Na-, Zn-, and Mg-ion batteries using vanadium oxides and in situ/operando analysis such as XRD, XAS, Raman, UV-vis, TEM, and AFM.[35–39]

2. In Situ/Operando XRD Analysis

XRD is based on the scattering of X-rays by periodically spaced lattices in a crystal.[40–43] XRD is used routinely to characterize and monitor the synthesis of battery materials, but it is also a powerful technique for operando monitoring of changes in the electrode material.[40–43] In situ/operando XRD analysis avoids the challenges with post-mortem XRD analysis of electrodes, such as changes of the electrode while retrieving them from the battery (e.g., short circuits) and changes to the material when exposed to air.[40–43] In situ/operando XRD analysis, on the other hand, can trace real-time phase changes and lattice parameter changes of electrode materials, which reveal additional insight into the energy storage and/or degradation mechanisms.[40–43] To measure in situ/operando XRD analysis, the cell designs should allow interaction with the X-ray beam while maintaining a perfect seal to prevent air and moisture contamination in the cell.[44–46] A further discussion of the design guideline for in situ/operando XRD cells as well as the operation of XRD can be found in the previous reports.[44–49] This section reviews papers conducting in situ/operando XRD analysis of batteries using different vanadium oxide formulations in LIBs, NIBs, ZIBs, and MIBs.

2.1. LIBs

2.1.1. V_2O_5

V_2O_5 has been widely used as a cathode material for LIBs due to its relatively high theoretical capacity of 294 mAh g^{-1} compared to other cathodes such as $LiCoO_2$ (≈140 mAh g^{-1}), $LiMnO_4$ (≈148 mAh g^{-1}), $LiFePO_4$ (≈170 mAh g^{-1}), $LiNi_{0.8}Mn_{0.1}Co_{0.1}O_2$ (≈279 mAh g^{-1}), and $LiNi_{0.8}Co_{0.15}Al_{0.05}O_2$ (≈274 mAh g^{-1}).[12,50–55] It is known that V_2O_5 has a typical layered structure, which is constructed by a periodic sequence of distorted VO_5 square pyramids (**Figure 2**a).[12] These layers of pyramids are stacked in the planes of (00*l*) with weak van der Waals interaction.[12] The intrinsic interlayer spacing is estimated at about 4.37 Å, possessing open ion diffusion channels between layers. This offers opportunities for intercalation of a range of different metal ions.[12] The Li$^+$ intercalation and de-intercalation process of V_2O_5 can be described as follows (Equation (1))

$$V_2O_5 + x\mathrm{Li} + xe^- \leftrightarrow \mathrm{Li}_x V_2O_5 \tag{1}$$

Figure 3a shows the potential profiles for the Li$^+$ intercalation and de-intercalation process of a V_2O_5 electrode at a current density of 50 mA g^{-1}.[19] These measurements show a 1st cycle discharge and charge capacity of 286 and 285 mAh g^{-1}, respectively, with a Coulombic efficiency of 99.7%. In addition, multiple plateaus in the potential profile during the discharging process correspond with Li$^+$ intercalation into the V_2O_5 layered structure, as explained below. To explore the structural evolution of V_2O_5 during discharge and charge, in situ/operando XRD analyses were performed at low rate of 0.05 C (Figure 3b).[19] Figure 3b shows the (001) peak shifts toward a lower diffraction angle from 3.5 and 3.0 V (vs Li/Li$^+$) during discharge (Stage 1). This shift was associated with the first transformation from pristine α-V_2O_5 to ε- and δ-$Li_xV_2O_5$ in the composition range of $0 < x < 1$.[50,56–59] When V_2O_5 was discharged to stoichiometries of $1 \le x < 1.3$ in the voltage window from 3.0 to 2.5 V (Stage 2), a sudden split of the (001) peak is observed. At this stage, the phase transformation from δ-$Li_xV_2O_5$ to γ-$Li_xV_2O_5$ proceeds while excess Li ions are inserted, where the VO_5 pyramids undergo an orientation change from "up–up" (denoted by the symbols "++") to up–down ("+–") (Figure 3c).[50,56–59] At stage 3, the intercalation of more than one Li ion ($1.4 < x$) leads to the transformation into ω-$Li_xV_2O_5$, where the plateau was observed from 2.5 to 2.0 V.[9,19] The peaks split from the (001) plane, merging to a peak toward the same position of the OCV state, indicating ω-$Li_xV_2O_5$, was going back to its pristine phase such as γ-, δ-, ε-, and α-V_2O_5.[35,50,56–59] This work investigated the changes of V_2O_5 such as lattice parameters, unit cell volume, and phases during a Li+ intercalation and de-intercalation. The intercalation of more than one Li$^+$ into V_2O_5 is a key consideration to further increasing the capacity of LIBs.

2.1.2. VO_2(B)

Monoclinic VO_2(B) is a promising cathode material for LIBs because of its unique layered structure, by edge-sharing VO_6 octahedra with cavities, which provides a direct pathway for Li ion transport into VO_2(B) (Figure 2b). Various nanostructured monoclinic VO_2(B) have shown improved electrochemical results.[15,60–64] To understand the enhanced electrochemical performance,

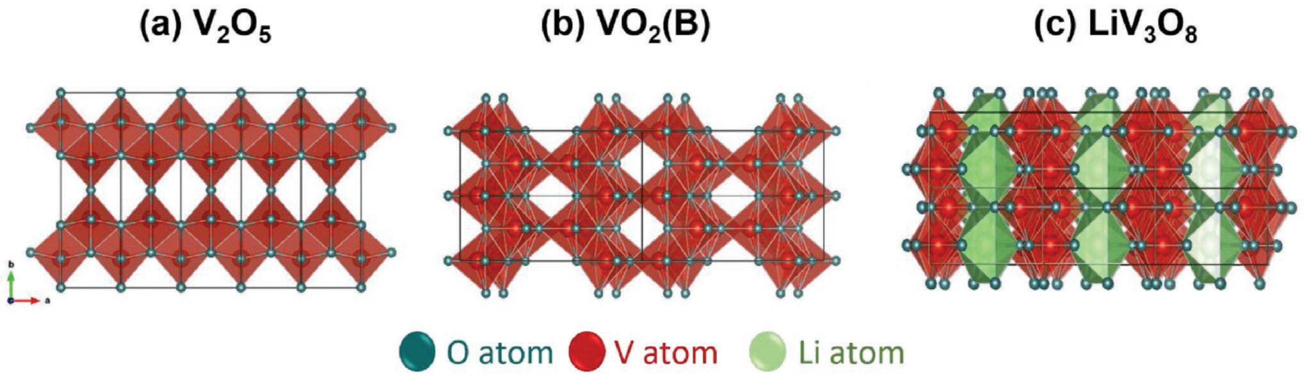

Figure 2. Schematic of the crystal structures of a) V_2O_5, b) VO_2(B), and c) LiV_3O_8 along the direction of the *c*-axis.

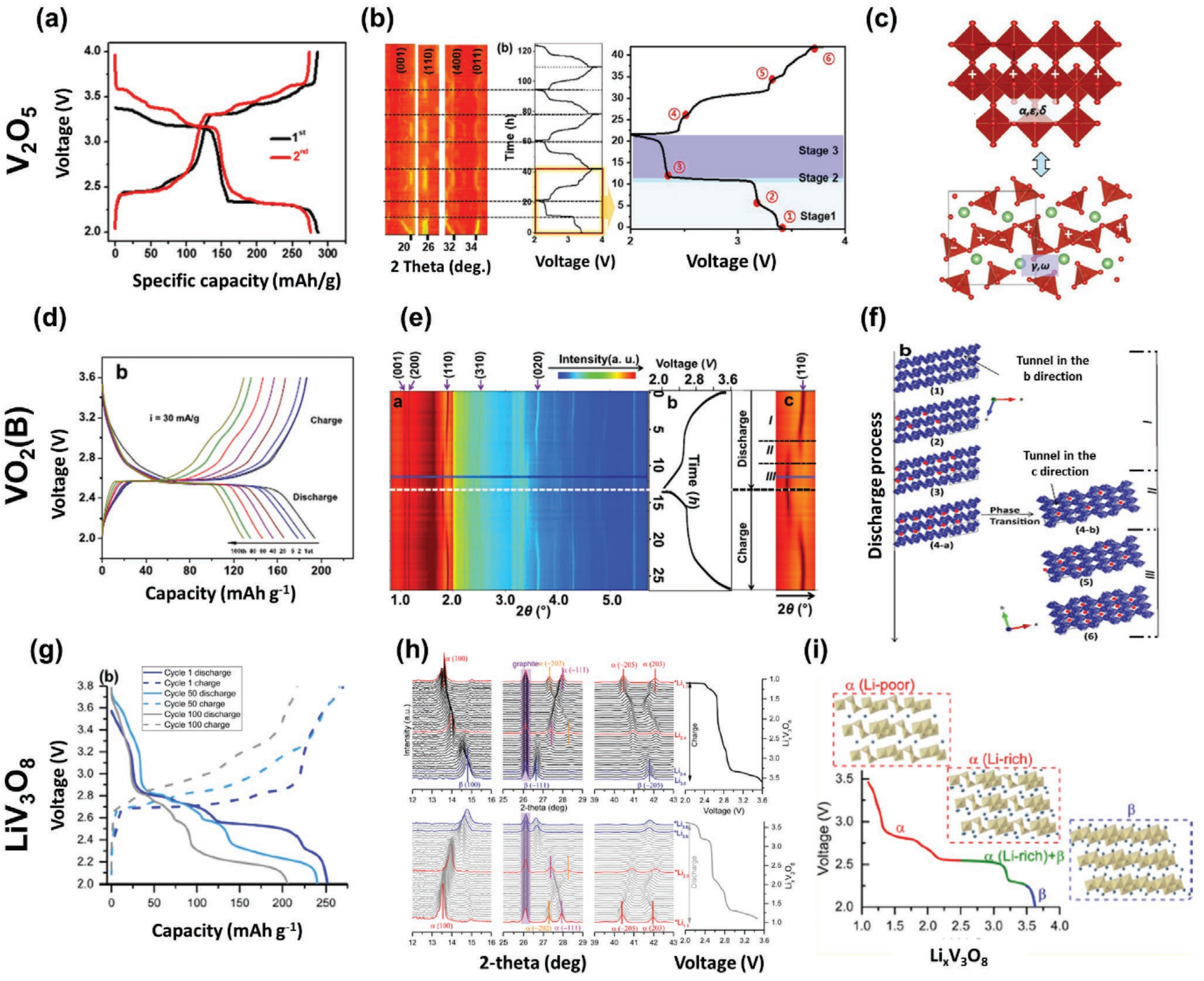

Figure 3. a) Discharge and charge curves of V_2O_5 at a current density of 50 mA g^{-1}. b) Contour plot of the in situ/operando XRD patterns of V_2O_5 during the discharge and charge processes, divided into three stages. c) Illustration of α, ε, δ, γ, and ω phases of orthorhombic V_2O_5. Red pyramids and green circles are V_2O_5 and Li ions, respectively. Reproduced with permission.[19] Copyright 2021, Elsevier. d) Discharge and charge curves, e) contour plot of diffraction patterns as a function of time and f) crystal structure of monoclinic VO_2(B) nanorods. Reproduced with permission.[15] Copyright 2018, Elsevier. g) Discharge and charge profiles of the LiV_3O_8 material cycled at C/10 between 3.8 and 2.0 V, h) expanded view of selected peak regions, i) crystal structures of LiV_3O_8, $Li_{2.5}V_3O_8$, and $Li_4V_3O_8$. Reproduced with permission.[27] Copyright 2017, American Chemical Society.

investigating the structural evolution during the discharge and charge processes is important. However, the electrochemical energy storage mechanism of VO_2(B) has not been studied extensively. Liu et al. reported Li ion insertion and de-insertion mechanism in monoclinic VO_2(B) nanorods via in situ/operando high-energy synchrotron XRD (HEXRD) (Figure 3d–f).[15] The voltage profile of VO_2(B) nanorods in the range of 2.0–3.6 V at a current density of 30 mA g^{-1} shows a pair of well-resolved cathodic and anodic voltage plateaus (Figure 3d). Figure 3e shows the 2D contour plot of the HEXRD patterns recorded at different discharge/charge states and the corresponding voltage profile. First, HEXRD patterns returned nearly to their OCV position after the first discharge and charge cycle, which indicates structural evolution is reversible. The discharge process can be divided into three different stages: I) During the discharge process, Li ions tend to be inserted into the largest sized tunnels first (i.e., the 8.2 Å^2 tunnel along the *b* direction) followed by the second largest tunnels (i.e., the 5.0 Å^2 tunnels along the *c* direction) (Figure 3f). In the initial discharge stage, the (110), (310), and (020) plane peaks move slightly to lower angles. These changes are minor, indicating that the insertion of Li ions into VO_2(B) nanorods does not significantly change the crystalline lattices of VO_2(B) without a phase transition, which corresponds to the sloping potential in discharge and charge curves as shown in Figure 3d. On the other hand, the (001) and (200) plane peaks are barely changed, indicating that the insertion Li ions in the largest tunnels along the *b* direction is favorable, which causes no significant lattice expansion. II) Next, at an intermediate state of discharge around 2.4 V, a wide-range plateau appears in the voltage profile and in the diffraction patterns the (110), (310), and (020) reflection splits into two peaks with the appearance of a peak at a lower angle, which corresponds to a new Li_yVO_2 phase. III) Finally, at deep discharge, only Li_yVO_2 remains and the (110), (310), and (020) peak position shifts continuously to lower angles as the discharge progresses, suggesting that the Li_yVO_2 lattice expands further as increasing amounts of Li ions are inserted in the material.

2.1.3. LiV_3O_8

LiV_3O_8 (LVO) is a monoclinic layered material that is a promising cathode material for LIBs because of its high-rate performance and relatively high theoretical capacity of 362 mAh g^{-1} (Figure 2c).[65–69] LVO has an excess vacant site in the interlayer of the layered structure, supporting the occupation of more ions.[66] Second, the weak Li—O bond, which arises from the lower electron density of the O^{2-} ions in the lattice, has been suggested to permit the hopping of ions and then a fast ion diffusion in LVO.[66–69] Zhang et al. reported the voltage profiles of the 1st, 50th, and 100th cycles to investigate the electrochemical stability of the LiV_3O_8 electrode, which shows capacity fade occurring predominantly around the 2.6 V plateau (Figure 3g–i).[27] This capacity fade is believed to be associated with a two-phase transformation process. To monitor these phase transformations, in situ/operando XRD was conducted during a full discharge and charge cycle in the range 3.6–2.0 V (Figure 3h). Figure 3h shows the evolution of the (110), ($\bar{2}02$), ($\bar{1}11$), ($\bar{2}05$), and (203) reflections during lithiation and delithiation. During lithiation from the Li-poor α-LiV_3O_8 to the Li-rich α-$Li_{2.5}V_3O_8$ (a = 6.54 Å, b = 7.58 Å, c = 12.15 Å, α = 89.87°, β = 104.04°, and γ = 90.03°), the (110) peak shifted to a higher angle, indicating the reduction in V_3O_8 interlayer spacing. The ($\bar{2}02$) and ($\bar{1}11$) peaks gradually crossed over: the ($\bar{2}02$) peak moved to a higher angle and the ($\bar{1}11$) peak moved to a lower angle to form the α- $Li_{2.5}V_3O_8$. At intermediate discharge to ≈2.6 V, corresponding to the $Li_{2.5}$ phase, new reflections emerge at 14.5° and 26.7°, respectively, corresponding to the β(100) and β($\bar{1}11$) of β-phase, while α-phase (100) reflections decreased in intensity, indicating a two-phase transformation. At the fully discharged state, the α-phase entirely transformed to β-phase, and the β(100) and β($\bar{1}11$) peaks shifted to a higher and lower angle, respectively. However, in situ data showed the V_3O_8 layer shrinks by 0.3 nm when transforming from $Li_{2.5}$ to $Li_{3.5}$ to form β-phase. The degree of contraction increased during cycling,[27] which could be linked to the capacity fade observed in the cycling tests.

2.2. NIBs

2.2.1. $NaVO_2$

Among various electrode materials for NIBs, layered vanadium oxides have gained significant attention owing to their high theoretical capacity and natural abundance. In addition, the vanadium oxides have sufficiently large interlayer spacing to accommodate Na ions, which are larger than Li ions into their lattice structure. However, vanadium oxides still suffer from poor ion diffusion coefficient, poor electronic conductivity, and large volume fluctuation.[21,65,70–72] To improve electrochemical performance of vanadium oxides for NIBs, recent studies have doped Na into the host material.[28,29,65,73–75] For instance, Claude's group synthesized the layered Na_xVO_2 systems and studied the structural transitions during intercalating and de-intercalation in NIBs with in situ/operando XRD experiments.[30,76] To understand the structural changes and the correlation with the electrochemical reaction of this material, shifts in XRD peaks are tracked in situ and are shown alongside electrochemical galvanostatic curves in **Figure 4**a. In the 0.67 > x > 0.50 composition range, the (002) peak shifts toward a lower diffraction angles as Na ions are de-intercalated. This corresponds to a gradual increase of the d-spacing ($2\cdot d_{(002)} = c\cdot \sin\beta$) due to increasing oxygen repulsions as the amount of Na ions decreases between the layers. In the 0.67 > x > 0.64 composition range, the (002) peak position shifts continuously to lower angles as the charge progresses. The (002) peak broadens between 2.10 and 2.23 V, which might be due to the existence of a bi-phase domain for the two phases.[76] A similar observation is made for the plateau between 0.62 > x > 0.55. The plateau shown in the 0.55 > x > 0.50 composition range from 2.27 V is the characteristic of the change from the two phases to single phase by the gradual change of the superstructure peaks intensities (Figure 4a,b). The presence of a superstructure is proof of a structural change from $NaVO_2$ to $Na_{1/2}VO_2$.

2.2.2. NaV_6O_{15}

NaV_6O_{15} can be formed by inserting one-third moles of Na^+ ions into V_2O_5 units (i.e., $Na_{1/3}V_2O_5$), where the preintercalated Na^+ ions between 2D V_4O_{12} layer act as pillars to stabilize the structure upon insertion/extraction of Na^+ ions.[28,29,77–79] In addition, these pillars enhance not only the interlayer space of materials but also the ion diffusion rate.[29,80,81] However, monitoring structural evolution of sodium vanadium oxides and corresponding understanding electrochemical performance in real time condition has not been explored much. Dong et al. reported structure evolution of NaV_6O_{15} electrode during Na^+ intercalation via in situ/operando XRD.[28] Figure 4c shows the voltage plateaus of the NaV_6O_{15} electrode between 2.7 and 3.0 V (vs Na/Na$^+$) during discharging and charging. In addition, even at current densities of 10 A g^{-1}, capacities of 96.5 mAh g^{-1} were retained (131.5 mAh g^{-1} at 0.1 A g^{-1}). To understand the reaction mechanism of $NaV_6O_{15,}$ in situ/operando XRD analysis was carried out (Figure 4d). The (200) plane gradually shifted to the lower angle during discharging while after charging, the (200) plane completely returned to the position of the open circuit voltage (OCV), where no new phase was observed. The high reversibility of the electrodes is attributed from single-phase charge–discharge mechanism during cycling, which causes good cyclic retention of 87% after 2000 cycles. In situ/operando XRD analysis of vanadium oxides for NIBs has still rarely reported. Therefore, more analysis needs to be done on other vanadium oxides as well to understand the structural and lattice evolution. In addition, organic electrolytes for NIBs tend to result in limited capacities, cycle stabilities, and rate capabilities. This is because of the low conductivity of the organic electrolyte and a lack of understanding of the Na-ion storage. For more details on the current challenges and developments on NIBs, we refer the readers to review papers such as.[6,13,75]

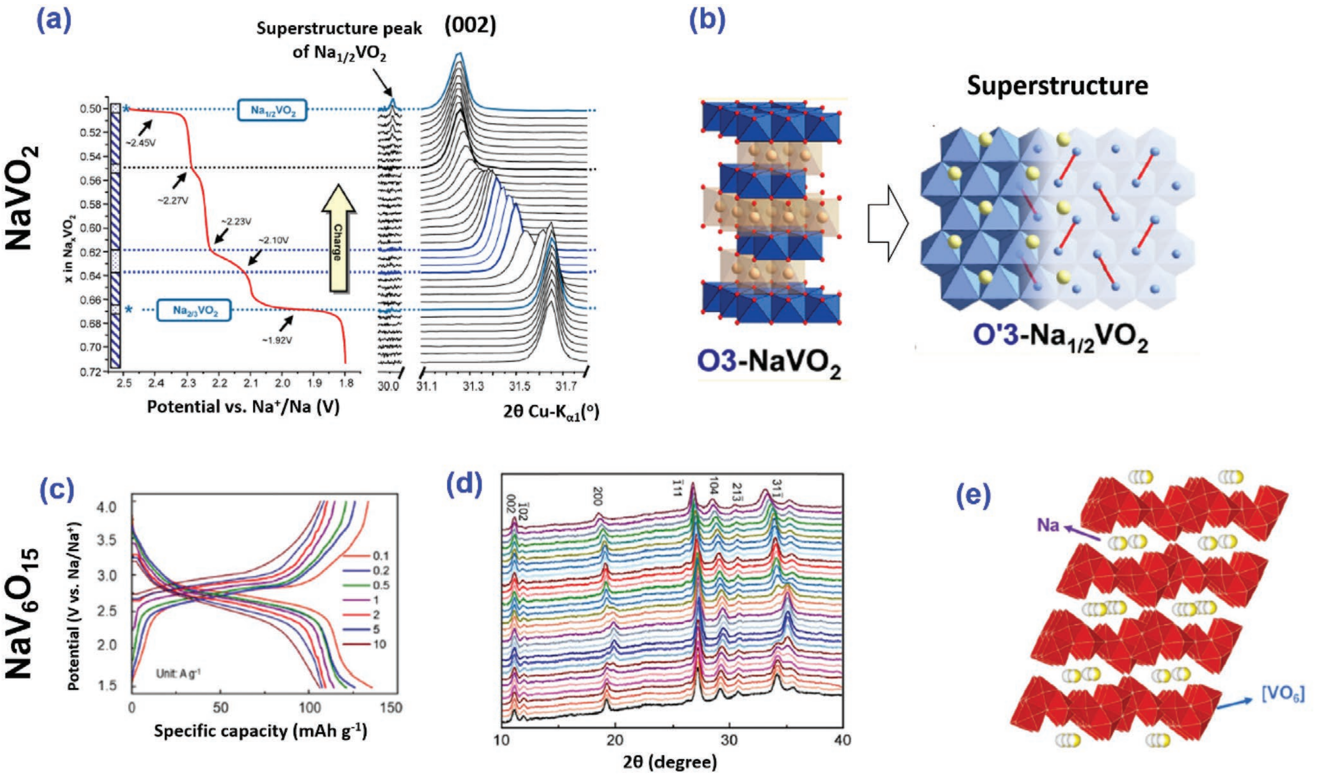

Figure 4. a) In situ/operando XRD obtained during charging process of $NaVO_2$. The evolution of (002) peak is aligned to the galvanostatic charge curve. b) Illustration of the structural change from $NaVO_2$ to $Na_{1/2}VO_2$. Reproduced with permission.[76] Copyright 2012, American Chemical Society. c) Charge and discharge curves of NaV_6O_{15}, d) in situ/operando XRD patterns during charging and discharging process of NaV_6O_{15}. e) Illustration of the crystal structure of typical NaV_6O_{15}, projection of NaV_6O_{15} along the *b*-axis, the connection way of $[VO_6]$ octahedral and $[VO_5]$ square pyramids, the sites occupied by sodium ions. Reproduced with permission.[28] Copyright 2021, Elsevier.

2.3. ZIBs

2.3.1. *$Zn_{0.25}V_2O_5{\cdot}nH_2O$*

Manganese-based oxides and Prussian blue materials have shown reversible Zn^{2+} intercalation and therefore have been investigated as cathode materials for ZIBs. However, these have some limitations in rate performance and specific capacity.[82–85] Kundu et al. reported that the $Zn_{0.25}V_2O_5{\cdot}nH_2O$ nanobelt possesses two-electron redox centers (vanadium) and a layered structure containing intercalated divalent cations and water, showing structural stability during cycling with high specific capacity.[82]

Ref. [86] shows the galvanostatic discharge and charge profile of a $Zn_{0.25}V_2O_5 \cdot nH_2O$ nanobelt at a current density of 300 mA g^{-1} in 1 м $ZnSO_4$, using a Zn anode. A capacity of 282 mAh g^{-1} is measured in the 1st discharge, corresponding to a 2.2 electron redox process, of which 278 mAh g^{-1} is recovered upon charging. In the subsequent 50 cycles, the voltage profile shows minor changes such as a small decrease in capacity, suggesting only slight structural changes. **Figure 5**a shows in situ/operando XRD measurement during the 2nd cycle to investigate the insertion mechanism in $Zn_{0.25}V_2O_5$. The discharge process can be separated into three different stages ($0.25 < x < 0.55$, $x \sim 0.55$, and $0.55 < x < 1.4$). Up to $x \sim 0.55$, there is only a slight contraction of the interlayer distance, consistent with an increased screening of the interlayer electrostatic repulsion as the inserted Zn^{2+} increases. From $x = 0.55$, the interlayer distance sharply contracts from 12.3 to 11.0 Å, which is similar to the 10.8 Å interlayer spacing observed in the pristine material before the H_2O intercalation from the electrolyte, which is attributed to the expulsion of water from the interlayer. In the $0.55 < x < 1.4$, the intensity and position evolution of the peaks at 26°, 32°, and 40°, clearly show that the structure continues to evolve during Zn^{2+} insertion.

2.3.2. *$VO_2(B)$*

$VO_2(B)$ has been used as a cathode material for ZIBs because of its layered and tunnel-type structure, which provides the benefit of fast intercalation and de-intercalation of zinc ions (0.74 Å).[14,86] The intercalation behaviors of $VO_2(B)$ in organic and aqueous electrolyte including Li and Na ions, have been widely investigated, while those in Zn^{2+} aqueous electrolytes are reported less.[14,63,87–89] Figure 5b shows a high and stable reversible capacity of 357 mAh g^{-1} was achieved at 0.25 C. To study the Zn^{2+} intercalation behavior into $VO_2(B)$ electrodes, Junwei et al. conducted in situ/operando XRD measurements, monitoring the structural change during the discharge and charge process (Figure 5c). The 2D contour map of the diffraction patterns collected during discharging exhibits a symmetric pattern to that during charging, suggesting a reversible

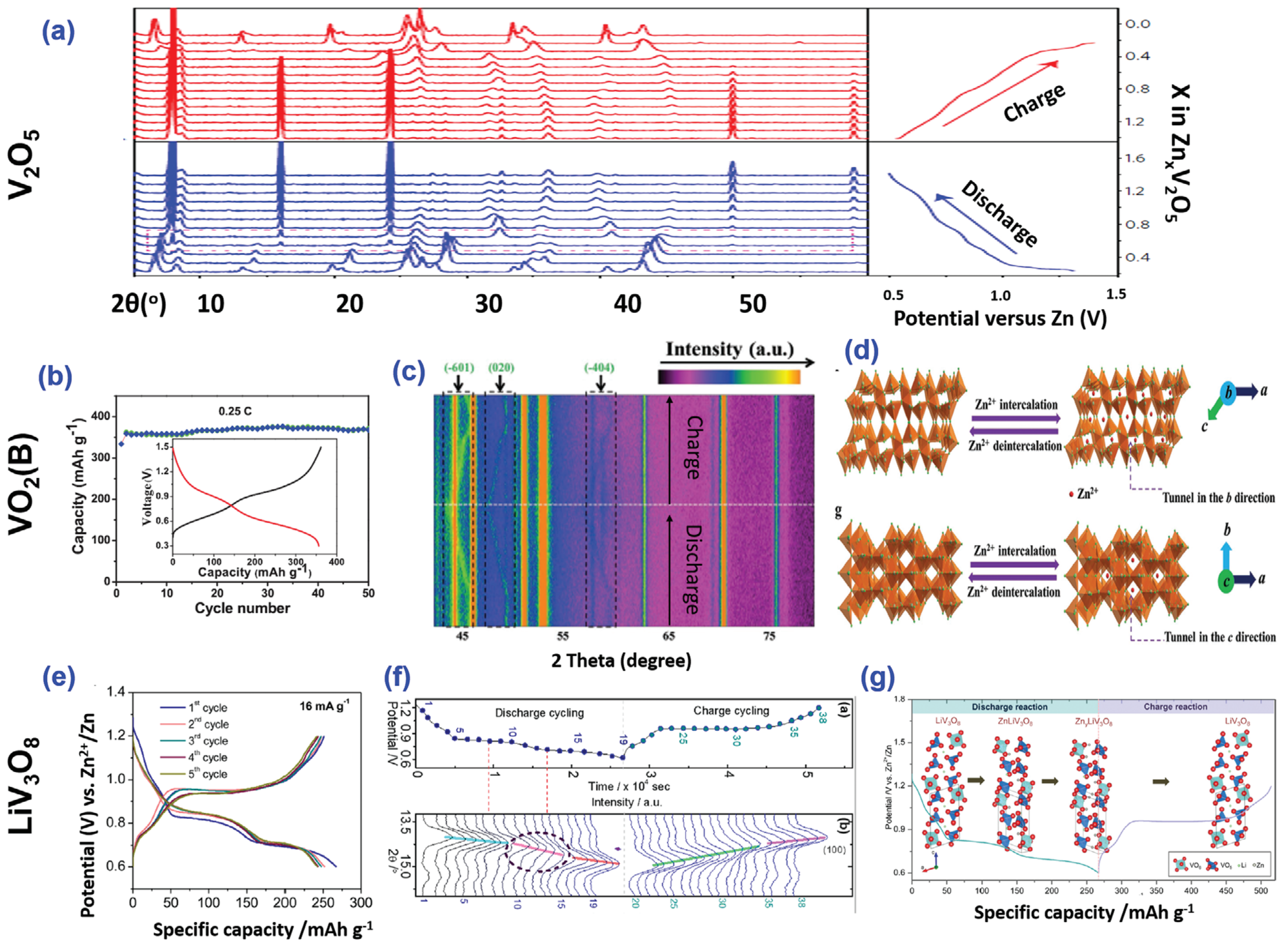

Figure 5. a) In situ/operando XRD measurement of the $Zn_{0.25}V_2O_5{\cdot}H_2O$ freestanding cathode during the second electrochemical cycle showing the evolution of the XRD patterns as a function of intercalated Zn^{2+} concentration. Reproduced with permission.[82] Copyright 2016, Springer Nature. b) Cycling performance of VO_2(B) nanofibers at 0.25 C (inset: typical galvanostatic charge-discharge curve). c) 2D contour map of in-situ/operando XRD peaks intensities versus galvanostatic charge and discharge times. d) Schematic view of Zn^{2+} intercalation/de-intercalation VO_2(B) nanofibers projected along the direction of the *b*- and *c*-axis. Reproduced with permission.[14] Copyright 2018, Wiley-VCH. e) Initial five voltage profiles of the LiV_3O_8 electrode at a current density of 16 mA g^{-1}. f) Electrochemical discharge profile of the fabricated spectro-electrochemical cell cycled within 1.2–0.6 V at a current rate of 16 mA g^{-1} and in situ/operando XRD patterns obtained within selected scanning angle (2*θ*) domains of 13.2–18°. g) Schematic of the Zn-intercalation mechanism in the present LiV_3O_8 cathode. Reproduced with permission.[66] Copyright 2017, American Chemical Society.

Zn^{2+} intercalation and de-intercalation into VO_2(B). During discharging from 1.5 to 0.3 V (vs Zn/Zn^{2+}), the (−601) and (−404) planes shifted to a lower angle, indicating the Zn^{2+} ions are simultaneously intercalated into the tunnel along the *b*-axis (Figure 5c and 5d). The (020) plane also moved from 49.2° to 46.9° 2*θ*, suggesting Zn^{2+} are gradually intercalated into the tunnel along the *c*-axis (Figure 5c). During charging from 0.3 to 1.5 V, these (−601), (020), and (−404) peaks return to their original positions, suggesting the tunnel structure of VO_2(B) is stable toward Zn2+ intercalation/de-intercalation.

2.3.3. LiV_3O_8

The layer structured LiV_3O_8 (LVO) is an interesting electrode material for ZIBs because of the fast ion diffusivity and structural stability.[66,69] As discussed above, LiV_3O_8 is a monoclinic layered material that is a promising cathode material for LIBs because of its high-rate performance and relatively high theoretical capacity of 362 mAh g^{-1}. In fact, the ionic radii of Li^+ and Zn^{2+} are similar at 0.76 and 0.74 Å, respectively, which indicates that the Zn^{2+} intercalation system of LVO is also possible.[66] Alfaruqi et al. synthesized a layered-type LVO as an intercalation cathode for ZIBs with high capacities. Figure 5e shows the discharge and charge curves at a current density of 16 mA g^{-1} in the potential range of 0.6–1.3 V. Two plateau regions were observed in the discharge curves, indicating Zn^{2+} intercalation. During the 1st discharge, the specific capacity for the Zn^{2+} intercalation is slightly higher than that during the de-intercalation of the 1st charge. However, from the 2nd cycle, the amount of intercalated Zn^{2+} is almost the same with that of de-intercalated Zn^{2+}. The phase and structural change of LVO was confirmed by in situ/operando XRD (Figure 5f). During discharge to 0.6 V, the evolution in (110) facet is significant because the lattice parameter "a" is largely influenced by the amount of Zn^{2+}. The discharge process can be divided into three regions. In the 1st region from 1.28 to 0.82 V, the (100) peak shifted to a higher angle, which is indicative of a single-phase domain displaying a solid-solution behavior, with a corresponding gradually sloping potential curve (Figure 5e–g). In the 2nd discharge region (0.81–0.7 V), the (100) peak splits into two peaks, which is attributed to the formation of a new Zn-rich phase like $ZnLiV_3O_8$ during Zn^{2+} intercalation. In the 3rd region for final discharge to 0.6 V, the (100) peak returns to a single peak, indicating a change from two-phase to a single-phase domain. During subsequent charging, the (100) peak does not entirely return to the same position as the pristine electrode, which relates to the difference in capacity the number and location of plateaus between the 1st charge and discharge process in the voltage profile (Figure 5e). This work suggests the formation of a stoichiometric $ZnLiV_3O_8$ phase with a maximum discharge capacity of 256 mAh g^{-1} at a current density of 16 mA g^{-1}.

2.4. MIBs

2.4.1. V_2O_5

MIBs have been considered as an alternative to replace LIBs because of various advantages of Mg metal such as abundance, low cost, and safety.[90–93] However, active electrode materials such as the Chevrel phase is suffering from slow ion diffusion.[90] V_2O_5 is used as a cathode material for MIBs because of its interstitial vacancies being large enough to insert Mg^{2+} ions into their layered structure.[90,94,95] However, the V_2O_5 capacity is limited to ≈180 mAh g^{-1} as electrodes for MIBs.[29,95–97] To understand this limited capacity, investigation of the structural changes of V_2O_5 in MIBs is crucial,[95] yet only few publications have been published on this topic to date. A recent paper provides information on the reversible crystal structure evolution and understanding the capacity of V_2O_5 nanowires for MIBs. **Figure 6**a shows the voltage profile of the V_2O_5 electrodes in a $Mg(ClO_4)_2$/AN electrolyte at C/20 during cycling. The 1st discharge curve exhibited a short plateau at around 0.9 V and a long plateau at around 0.4 V while only one flat plateau is observed at around 1.1 V for the 1st charge curve. In addition, the capacities at 1st discharge and charge were 103 and 110 mAh g^{-1}, respectively. The 2nd cycle also shows a similar behavior with a lower plateau compared with that of the 1st discharge. The 5th cycle shows a different voltage profile and an enhanced capacity compared with that of 1st and 2nd cycles, which might be attributed to an irreversible phase change during cycling. To understand the electrochemical mechanism during the 1st and 2nd cycles, in situ/operando XRD was performed. Figure 6b shows contour maps in the selected ranges during the first two cycles. In the initial part of the first discharge, $Mg_{0.14}V_2O_5$ is formed (region I). As discharging progresses, most peaks such as (200), (101), (400), (001), and (301) shifted to lower angles, indicating an expansion of the unit cell from gradual Mg^{2+} insertion (Figure 6b,c). At the end of discharge, new reflections appear while those from the $Mg_{0.14}V_2O_5$ phase decreased, indicating that a new phase like $Mg_{0.6}V_2O_5$ with Mg-rich $Mg_{0.49}V_2O_5$ is present (region II). During charge process, the intensities of the Mg-rich phase gradually decreased while intensities of Mg-poor phase increased. The positions of these reflections remained at a slightly lower angle than that for the OCV state, which is in agreement with the capacity irreversibility discussed above (Figure 6a). This paper reported the structural change for only the first and second cycle, and it would be interesting to analyze the structure of the material after the fifth cycle.

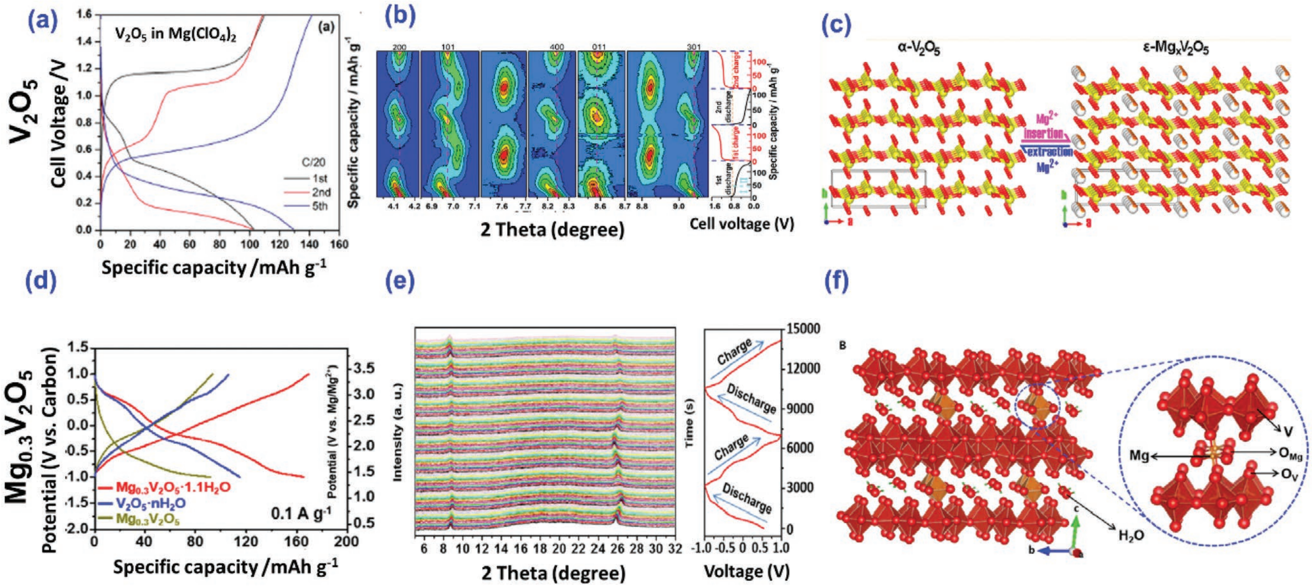

Figure 6. a) Discharge and charge profile of V_2O_5 in $Mg(ClO_4)_2$/acetonitrile (ACN) electrolyte, b) contour maps of in situ/operando synchrotron diffraction of V_2O_5 collected during the first two discharge and charge processes and the corresponding discharge and charge profiles at C/25 at a cell voltage of 0.01–1.6 V. c) Illustration of Mg^{2+} insertion/de-insertion V_2O_5 along the direction of an axis. Reproduced with permission.[90] Copyright 2019, American Chemical Society. d) Charge–discharge curves of $Mg_{0.3}V_2O_5$·1.1H_2O. e) In situ/operando XRD patterns of $Mg_{0.3}V_2O_5$·1.1H_2O during the first two electrochemical cycles showing the structural evolution as a function of intercalated Mg^{2+} concentration. f) Schematic diagram of the crystal structure of $Mg_{0.3}V_2O_5$·1.1H_2O. Reproduced with permission.[24] Copyright 2019, Elsevier.

2.4.2. $Mg_{0.3}V_2O_5$

$V_2O_5 \cdot nH_2O$ has been studied as a cathode material for MIBs because of the shielding effect of water makes the cation insertion into the host material easier.[24,98,99] However, their rate capability and cycle life are limited due to poor electrical conductivity and poor structural stability, resulting from larger interlamellar spacing due to excess water between layers.[24,82,100,101] To overcome these limitations, Xu et al. developed a Mg^{2+} preintercalated hydrated vanadium oxide ($Mg_{0.3}V_2O_5 \cdot 1.1H_2O$).[24] In addition, this work studies the structure and reaction mechanism via in situ/operando XRD. The charge and discharge curves of the electrodes at a current density of 100 mA g^{-1} in the potential range of 1.4–3.4 V (vs Mg/Mg^{2+}) are shown in Figure 6d. For the discharge curve, three plateaus were observed at around 3.02, 2.25, and 1.40 V, which is indicative of a multistep Mg^{2+} intercalation behavior in the layer structure. The discharge capacity of $Mg_{0.3}V_2O_5 \cdot 1.1H_2O$ is 164 mAh g^{-1}, corresponding to 0.5 Mg^{2+} ions per formula unit, which is higher than the 114 and 91 mAh g^{-1} reported for $V_2O_5 \cdot nH_2O$ and $Mg_{0.3}V_2O_5$, respectively. In addition, $Mg_{0.3}V_2O_5 \cdot 1.1H_2O$ exhibits higher cycling performance compared with $V_2O_5 \cdot nH_2O$ and $Mg_{0.3}V_2O_5$. In situ/operando XRD analysis was employed to investigate the crystal structure evolution of $Mg_{0.3}V_2O_5 \cdot 1.1H_2O$ during charging and discharging (Figure 6e). During discharging, the main (001) diffraction peak at 8.7° 2θ shifted slightly to a higher angle as Mg^{2+} is intercalated into electrode material. Meanwhile, the (003) reflection also moved toward a higher angle from 25.7° to 26.5° 2θ. At a full discharge state, the interlayer spacing of layer $Mg_{0.3}V_2O_5 \cdot 1.1H_2O$ decreased from 11.9 to 11.4 Å, which represents a small lattice change of 4.2%. It is derived from a benefit of the pillaring effect of the preintercalated Mg^{2+} to maintain structural stability. During the following charge process, the interlayer spacing and peak position showed a full recovery from Mg^{2+} extraction. In addition, in situ/operando XRD patterns for the 2nd discharge and charge demonstrated the high reaction reversibility and stable crystal structure.

3. In Situ/Operando X-Ray Absorption Spectroscopy (XAS)

XAS is used to determine the local geometric and/or electronic structure of materials. The technique can be divided into XANES and EXAFS. XANES provides information on the chemical state of the absorbing atoms, local symmetry, and chemical bonding, while EXAFS is sensitive to the spatial arrangements of nearest neighbors around the absorbing atoms. Since these experiment usually requires synchrotron X-rays, there are fewer examples of in situ/operando XAS studies of vanadium oxide battery materials than for XRD, which can be performed both on lab-based instruments and at synchrotrons. Compared to ex situ measurements, in situ/operando XAS offers similar advantages as for XRD, namely, measurement without sample exposure and the possibility to measure several points during electrochemical cycling using a single sample thus avoiding subtle differences in sample preparation. Thus, in situ/operando XAS can provide more reliable and precise data for analysis. In situ/operando XAS cells are very similar to those for XRD analysis. However, XAS analysis is mostly measured in the transmission mode.[44,102,103] Therefore, the cells should be designed with two X-ray transparent windows at the top and bottom of the cell and thick electrode. Further details on these cells as well as the principles of XAS are provided in other papers.[44,46–49,102,103] This section reviews papers conducting in situ/operando XAS analysis of vanadium oxide-based cathodes in LIBs, ZIBs, and MIBs.

3.1. LIBs

3.1.1. V_2O_5

During lithium insertion into V_2O_5, the position of the XANES main edge continuously shifts to a lower binding energy which is indicative of a decrease in the average valence state of vanadium (**Figure 7**a).[104–107] Comparison of the edge position with standards (crystalline V_2O_5, VO_2, and V_2O_3 for V^{5+}, V^{4+}, and V^{3+}, respectively) shows that pentavalent vanadium is initially reduced to tetravalent vanadium during the intercalation of 0–2 Li^+ per V_2O_5, and then tetravalent vanadium is reduced to trivalent vanadium upon additional insertion of Li^+.[106] In the fully discharged state, a shoulder emerges—red arrow in Figure 7a—which is consistent with the reduction of tetravalent vanadium to trivalent vanadium.[104–106] The pre-edge peak also shifts to lower energy upon lithiation in response to the decreasing oxidation state of vanadium.[106,107] Simultaneously, the pre-edge peak decreases in intensity. Within a specific coordination geometry, the area under the pre-edge peak shows a strong dependence on the oxidation state and local structure of vanadium, such as the degree of local distortion of the first coordination sphere. Therefore, in the reduced state the local structure of vanadium has a higher degree of octahedral symmetry.[106,107] Mansour et al. gave a detailed analysis of the EXAFS during the first discharge of V_2O_5.[106] The first peak in the Fourier transform in the 1–2 Å range is related to the first shell V–O coordination, and the second peak in the 2–3 Å range to the second shell V–V coordination.[106,107] While the V–O distance remains relatively unchanged during lithiation, the increasing amplitude of the first shell coordination indicates an increasing degree of local symmetry and hence a narrower range of V–O distances. There are significant and complex changes to the second shell V–V coordination, but overall the V–V distance decreased with increasing lithium content in line with the changes seen between standards V_2O_5, VO_2, and V_2O_3, i.e., transitioning from pentavalent to tetravalent to trivalent vanadium oxidation state.[106] The significant changes in the local geometry upon lithium intercalation are proposed to be a key contributor to the poor cycle life of V_2O_5. Unfortunately, Liu et al. do not include EXAFS analysis for their reported graphene-modified nanostructured vanadium pentoxide hybrids.[104,105] Finally, on the first cycle the changes in the XANES for V_2O_5 are reported to be highly reversible.[104,105,107] Upon charge, the energy shifts of the pre-edge peak and main edge, and the intensity of the pre-edge peak, return very closely to their original value indicating good electronic reversibility in the first cycle.

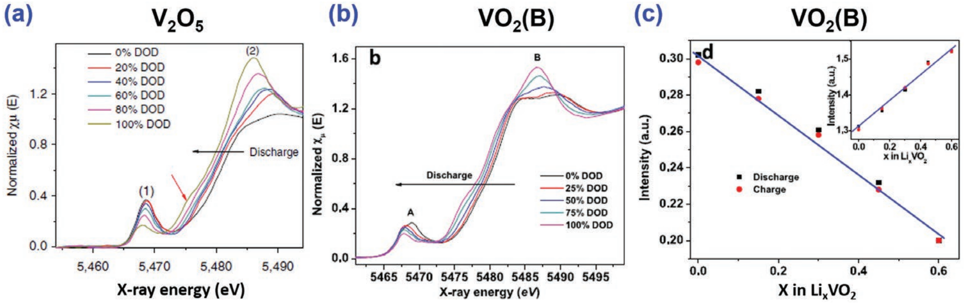

Figure 7. a) In situ/operando XANES spectra at the V K-edge of a V_2O_5-graphene cathode during the first discharge process.Reproduced with permission.[104] Copyright 2015, Nature Communications. b) In-situ/operando XANES spectra at the V K-edge characterization of VO_2(B) during the first discharge process.[15] c) Dependence of intensity of the XANES pre-edge and edge resonance (main peak, inset) on composition in the first charge/discharge cycle.[15]

3.1.2. $VO_2(B)$

XANES spectra collected during lithium insertion into VO_2 (B), with a starting V^{4+} oxidation state, also reveal a continuous shift of the main edge toward a lower binding energy (Figure 7b).[15,111] As was also seen for V_2O_5, a shoulder forms in the main edge and pre-edge nearing the discharged state, confirming the presence of both tetravalent and trivalent vanadium oxidation states concurrently.[15,36] The pre-edge also decreases in intensity, as was seen for V_2O_5, indicating a higher degree of local symmetry.[15,36] The shift in the main edge is found to be morphology dependent, with VO_2 with a smaller particle size (made by microwave-assisted synthesis) yielding a greater shift in edge position—i.e., greater reduction of V^{4+}—and higher discharge capacity compared to VO_2 from solvothermal synthesis.[36] Linear combination analysis (LCA) using VO_2 and V_2O_3 standards shows the valance state changed from V^{4+} to $V^{3.4+}$, equivalent to a lithiation capacity of 194 mAh g^{-1} and consistent with the reported electrochemistry.[15] Trends in the XANES spectra collected on the first and second cycles, e.g., the edge position and the intensity of the pre-edge and resonance peak as shown in Figure 7c, show good early reversibility of the VO_2 electronic structure.[15] Unfortunately, to our knowledge, there has been no thorough in situ investigations of the EXAFS for VO_2 during Li intercalation and de-intercalation.

3.2. ZIBs

3.2.1. V_2O_5

Zhao et al. used in situ/operando XAS to investigate NH^{4+} pre-intercalated $V_2O_5\cdot nH_2O$ as a cathode for aqueous rechargeable Zn-ion batteries.[108] Despite the different electrolyte system, the trends in the XANES during intercalation of Zn^{2+} into V_2O_5 (1 M $ZnSO_4$ electrolyte) are similar to that described above for Li^+ intercalation in organic carbonate-based electrolyte (e.g., 1.2 M $LiPF_6$ in ethylene carbonate (EC) and ethyl methyl carbonate (EMC) 3:7 by weight). In brief, during Zn^{2+} intercalation the main edge and pre-edge shift to lower energies and the pre-edge decreases in intensity; these changes are reversed on Zn^{2+} extraction during charge (**Figure 8**a,b). As expected, the changes in the EXAFS reveal a strong perturbation of the local structure around vanadium during Zn^{2+} intercalation (Figure 8c,d). An increase in the amplitude of the first shell V–O again highlights the increasing symmetry during vanadium reduction. In contrast to Li^+ insertion into V_2O_5, which showed the greatest change in the second shell V–V feature, Zn^{2+} insertion mainly affects the first V–O shell structure, inducing a shift to lower radial distances while the V–V shell structure only shows changes in intensity.

3.2.2. $VO_2(B)$

The same groups represented in ref. [108] also reported in situ/operando XAS of Zn^{2+} insertion/de-insertion with a VO_2 (B) cathode in aqueous 1 M $ZnSO_4$ electrode.[109] Again, the trends in the XANES (Figure 8e) closely reflect those for Li^+ insertion, namely, the pre-edge and main edge shift toward lower energy as tetravalent vanadium is reduced to trivalent vanadium and the pre-edge decreased in intensity with the increase in local symmetry. LCA with VO_2 and V_2O_3 standards suggests reduction of V^{4+} to $V^{3.26+}$ and a fully discharged composition of $Zn_{0.37}VO_2$, which is consistent with the 255 mAh g^{-1} of capacity measured in the electrochemistry (i.e., $V^{3.21+}$ and $Zn_{0.395}VO_2$). Zn^{2+} insertion into VO_2 strongly modifies the local structure, as shown in the phase uncorrected Fourier transform EXAFS spectra in Figure 8f. The V–O feature increases in intensity and shifts to shorter radial distances indicating a higher degree of symmetry and shorter V—O bond length, while the V–V coordination sphere shows changes in shape and position reflecting structural changes due to Zn^{2+} intercalation.

3.3. MIBs

3.3.1. V_2O_5 and $Mg_{0.3}V_2O_5$

In situ/operando XAS of vanadium oxides in MIBs has been reported recently for V_2O_5.[90] The pre-edge and main edge progressively shift to lower energy on discharge (**Figure 9**a) and the reverse occurs on charge (Figure 9b), indicating the reversible reduction of pentavalent vanadium and the

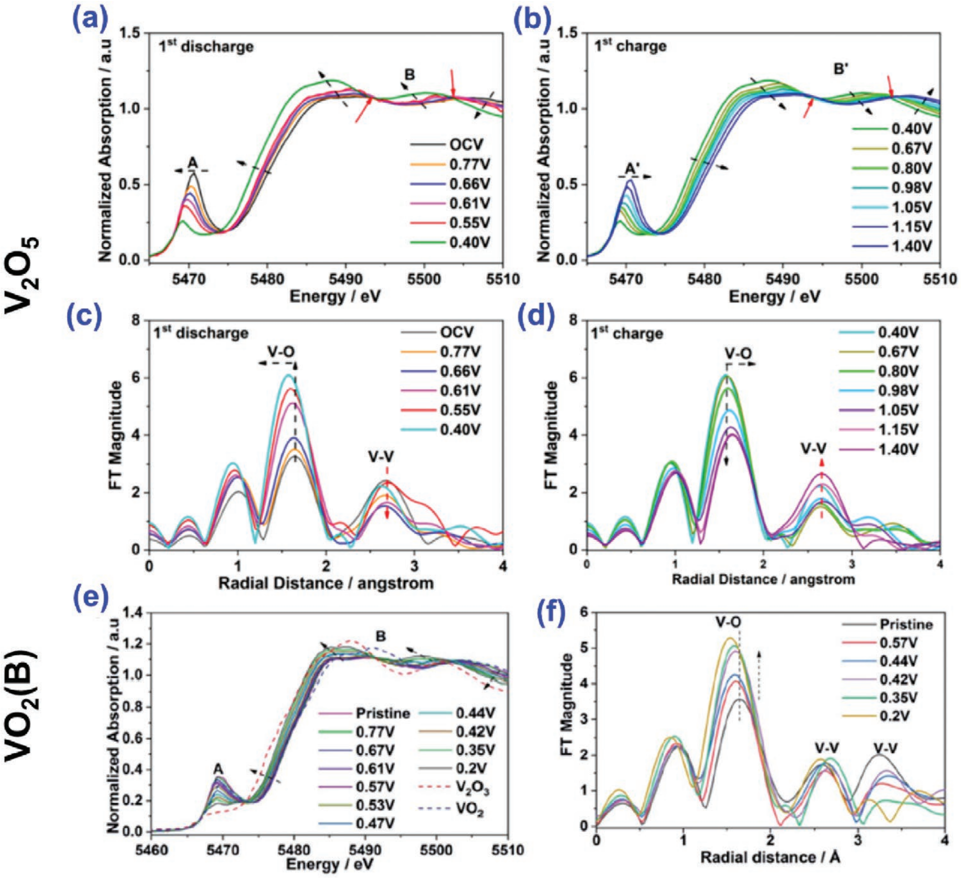

Figure 8. V K-edge XANES of the NH^{4+} preintercalated V$_2$O$_5$·nH$_2$O electrode during a) discharge and b) charge processes. Fourier transforms of V K-edge EXAFS (k^3-weighted) during c) discharge and d) charge processes. Reproduced with permission.[36] Copyright 2020, American Chemical Society. e) In situ/operando V K-edge XANES spectra of the VO$_2$(B) electrode during discharge, and f) Fourier transforms (k^3-weighted) of the V K-edge EXAFS as a function of state of discharge. Reproduced with permission.[108] Copyright 2020, Royal Society of Chemistry.

insertion/de-insertion of Mg^{2+} with V$_2$O$_5$. In the discharged state, the edge position is stated to be “in the middle between that of standards V$_2$O$_3$ and V$_2$O$_5$” and closely matches VO$_2$, although the reported discharge capacity suggests a composition of Mg$_{0.51}$V$_2$O$_5$ and vanadium oxidation state closer to 4.5+. In LIBs and ZIBs, the pre-edge feature for both V$_2$O$_5$ and VO$_2$ showed a significant decrease in intensity in the discharged state—see Figures 7a,c and 8b,e, respectively.[104–108] By comparison, the pre-edge intensity changes very little during Mg^{2+} insertion into V$_2$O$_5$ (Figure 9a,b), which is possibly related to the lower degree of vanadium reduction for Mg^{2+} insertion (from electrochemistry: V$^{4.5+}$) compared to Li$^+$ (V$^{3.5+}$) and Zn^{2+} (between V^{3+} and V^{4+}).[90,104,105,108] The in situ/operando EXAFS spectra are not reported in ref. [90], although ex situ data for a Mg$_{0.3}$V$_2$O$_5$·1.1H$_2$O cathode (pristine composition) discharged to 164 mAh g^{-1} or the equivalent of ≈0.5 Mg^{2+} per formula unit has been recently reported by Xu et al.[24] The Fourier transform EXAFS spectra in Figure 9d (with corresponding XANES in Figure 9c) show an increase in the length of the V—O bond while the V—V distance marginally shortens, which again shows much milder changes in the local structure compared to that seen in LIBs and ZIBs.

4. In Situ/Operando Raman

4.1. LIBs

Raman spectroscopy is a powerful technique for detecting variations in local disorder, bond lengths, and bond angles.[41,110] The cells for in situ/operando Raman need to be designed with a window for laser light to reach the electrode.[44,73,74,111] A more detailed description of cell designs and the use of Raman for batteries can be found in refs. [44,73,74,111]. Baddour et al. reported the effect of Li insertion/de-insertion into orthorhombic crystalline V$_2$O$_5$ thin films using in situ/operando Raman spectroscopy.[109] **Figure 10**a shows the discharge–charge curve of V$_2$O$_5$ from 3.8 to 2.8 V at a C/3 rate, which exhibits two well-defined insertion processes at about 3.4 and 2.3 V. In addition, this insertion and de-insertion reaction is reversible with a high Coulombic efficiency around 99%. To confirm the change of the local structure for the insertion/de-insertion of Li into V$_2$O$_5$, in situ/operando Raman analysis was studied as shown in Figure 10b,c. An assignment of the Raman spectrum has been previously reported on the local structure of V$_2$O$_5$ characterized by a coordination of vanadium with oxygen.[110,111] A

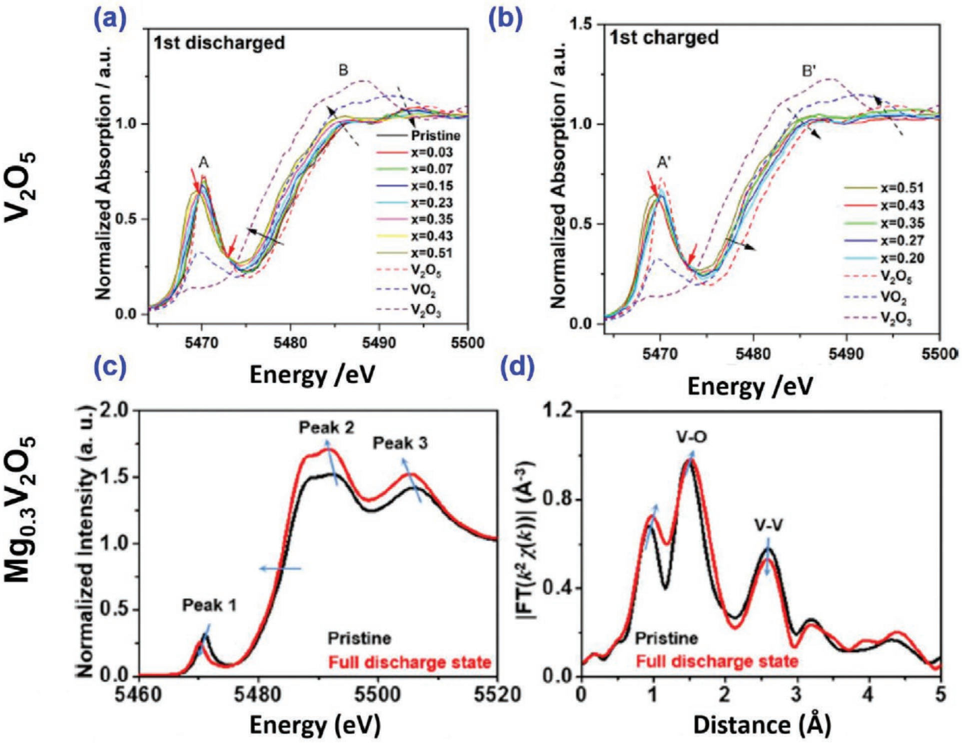

Figure 9. a,b) In situ/operando XANES for the V K-edge during the first discharge and charge process; the isosbestic points are indicated by red arrows. Reproduced with permission.[90] Copyright 2019, American Chemical Society. c,d) V K-edge XANES spectra of $Mg_{0.3}V_2O_5 \cdot 1.1H_2O$ and the corresponding Fourier transform extended X-ray absorption spectroscopy (FT-EXAFS) spectra in R space. Reproduced with permission.[24] Copyright 2019, Elsevier.

complete recovery of the Raman spectrum was shown after the insertion and de-insertion of Li ions (Figure 10b,c). The following observations were made in the $0 \leq x \leq 0.94$ composition range of $Li_xV_2O_5$:

1) A decrease in the intensity at 145 cm^{-1} and a peak shift from 145 to 153 cm^{-1} are observed, which corresponds to an increase of disorder within the V_2O_5 layer as Li ions are inserted.
2) Several modes at 404 and 527 cm^{-1} shift toward higher wavenumber, which is consistent with a stiffening of the lattice along the *a* direction, where the displacement of oxygen takes place.
3) The vanadyl stretching mode of pristine V_2O_5 is observed at 997 cm^{-1}. During Li insertion, this V—O stretching mode shifts to 980 cm^{-1}. It suggests the spacing in the layers in the *c* direction has increased. In addition, a new peak is observed at 958 cm^{-1} at higher Li insertion levels ($x \geq 0.75$), which is related to the formation of a new Li-rich phase.[110] The above bond changes such as intensity and location return to the original state after Li insertion and de-insertion. Baddour et al. reported in situ/operando XRD analysis only for the first cycle. However, investigations into multiple cycles are also very important to confirm reversible structural change of V_2O_5. Zhang et al. studied in situ/operando Raman during insertion and de-insertion of Li ions into V_2O_5 nanowire for four cycles[43] Figure 10d,e shows the in situ Raman test for four cycles (voltage window 2.0–4.0 V, current density 100 mA g^{-1}) and it is observed that the peaks that represent б(O3–V–O2), ν(d3) and ν(d1), which are at around 200, 700, and 1000 cm^{-1}, decrease rapidly with cycle number. This may suggest the distortion of crystallinity of the local structure of V_2O_5. Further, the Raman band at around 980 cm^{-1} shift toward lower wavenumbers and widen, which means that Li insertion into V_2O_5 expands the shortest V—O bond along the *b* axis.

4.2. ZIBs

Mai and co-workers measured in situ Raman to evaluate the structural transformation of V_2O_5 cathode during intercalation and de-intercalation of Zn ions and **Figure 11**a shows the schematic illustration of the measurement set up.[37] As shown in Figure 11b (third charge/discharge curve in voltage range of 0.3–1.4 V and respective Raman spectra at different state of charge), particularly the intensities of the Raman peaks associated with vanadyl oxygen stretching mode (≈1034 cm^{-1}) and doubly coordinated oxygen stretching mode (≈766 cm^{-1}) increase during charging process (de-intercalation of Zn ions), and then gradually decreases when discharged to 0.3 V. The insertion of Zn ions into layered V_2O_5 weakens the intensity of the Raman signals and the Raman signal is reversible when de-intercalating Zn ions from V_2O_5. This suggests that the electron transfers in the redox couple of V^{5+} and V^{4+} are reversible during the discharge and

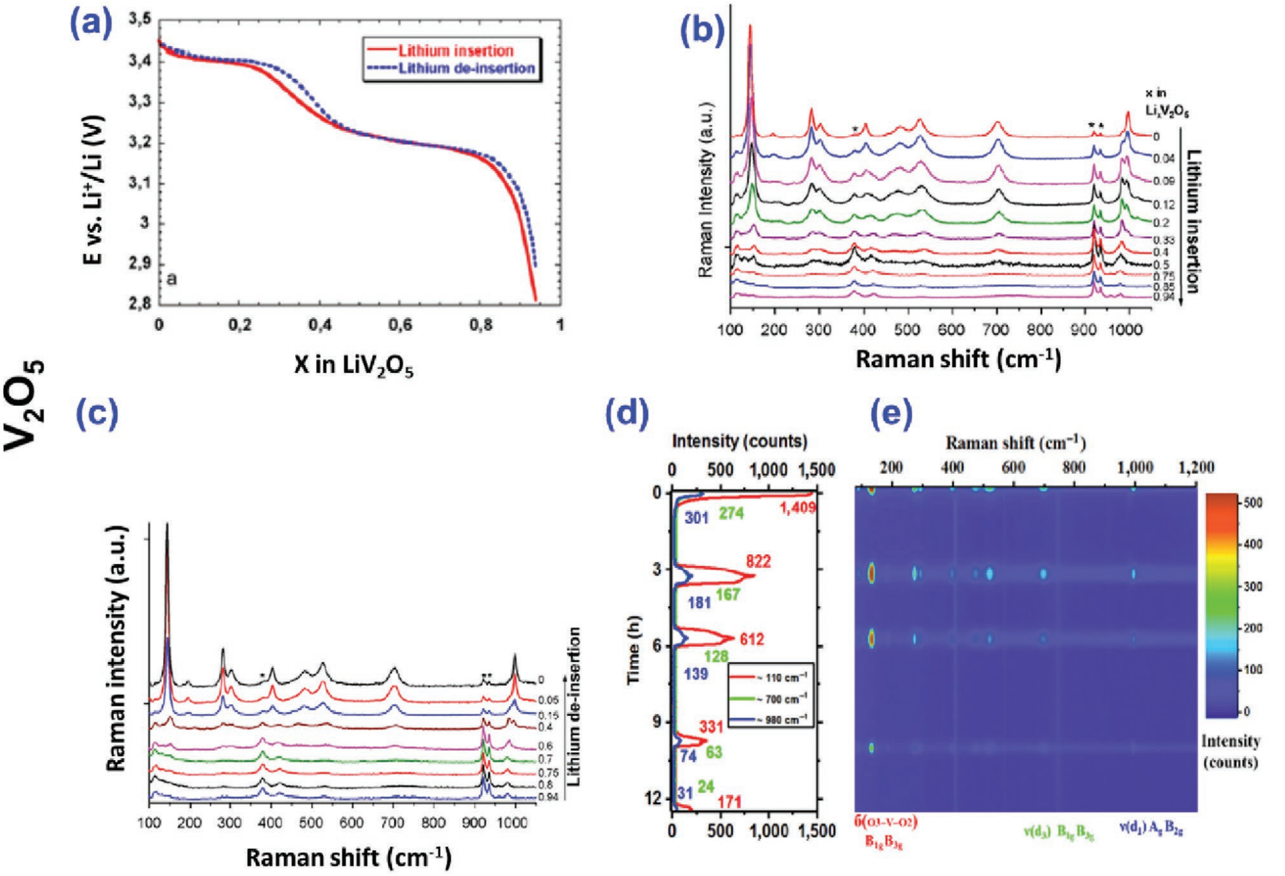

Figure 10. a) First discharge and charge profile of a V_2O_5 at C/3 rate in 0.7 M $LiClO_4$/ACN. b,c) In situ/operando Raman spectra series of the first discharge and charge process of a $Li_xV_2O_5$. $0 \leq x \leq 0.94$. (*) $LiClO_4$ in ACN bands. Reproduced with permission.[109] Copyright 2009, Elsevier. d,e) In situ/operando Raman spectra of V_2O_5 for four cycles at a current density of 100 mAh g^{-1}. Reproduced with permission.[43] Copyright 2019, Springer Nature.

charge. Further, Li et al. studied in situ Raman of the $K_2V_3O_8$ cathode in ZIB system at different states of charge.[112] It is observed that the intensity of the characteristic band located around 891, 926, 464, and 526 cm^{-1} assigned to the $K_2V_3O_8$ cathode change noticeably in charge and discharge processes. For instance, the peaks intensities first weaken and then reach a maximum at the end of the charge stage as shown in Figure 11d,e. This change of peak intensities is related to the deformation of the [VO_4] tetrahedron and the [VO_5] pyramids.[112,113] It is attributed from the extraction of K^+ in the first charge.

5. In Situ/Operando Combined Optical Characterization and UV-Vis, TEM, and AFM of V_2O_5

The optical characterization and UV-vis measurements of V_2O_5 have been carried out to understand changes in the bandgap of these materials as a function of their state of charge. This is important for applications in light rechargeable batteries which have been demonstrated for V_2O_5 in both LIB[38] and ZIB[114] systems. As illustrated in **Figure 12**a,b, the color of V_2O_5 changes from orange to light gray when discharged to 2 V which implies changes in the optical properties of V_2O_5. The UV-vis analysis (Figure 12c) suggests that insertion of Li ions into V_2O_5 increases the bandgap followed by shifting the optical absorption peak toward higher energies. The design of in situ/operando cell was shown in refs. [38,44]. It was mentioned earlier that the phase transformation from the α-phase into ε-phase undergo when insertion of Li ions into V_2O_5 that results alter the bandgap of V_2O_5 photocathode. It is important to note that the insertion of Li ions into V_2O_5 moves up the Fermi energy level near to the split-off band of V_2O_5, which expands the optical bandgap energy (E_{gLi}) of V_2O_5 followed by the relation of $E_{gLi} = E_g + E_{g1}$, where E_g denotes the optical band gap of pristine V_2O_5 and E_{g1} represents the Burstein–Moss shift.[115,116] This change in the optical properties of V_2O_5 under Li ions insertion is reversible, where the Li ions inserted light gray colored V_2O_5 changes to its original orange color when extracting Li ions (Figure 12b). In comparison, VO_2 (B) ZIB electrodes did not show significant changes in optical properties as a function of the state of charge based on ex situ measurements.[117]

Gu et al. probed the insertion/de-insertion behavior of Li ions in V_2O_5 nanoribbons by in situ/operando TEM. For in situ/operando TEM analysis, it is the important to keep the

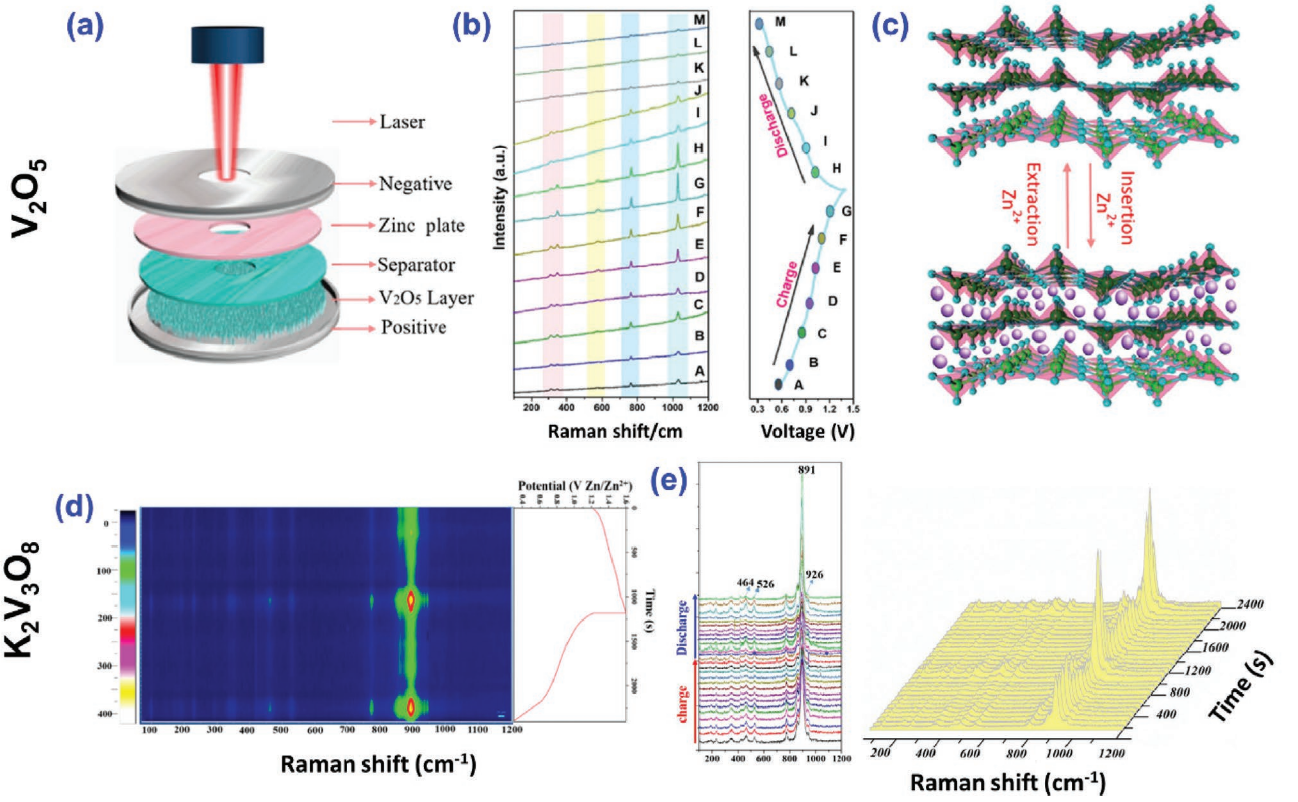

Figure 11. a) Schematic illustration for the testing set-up of in situ Raman spectroscopy. b) In situ/operando Raman spectroscopy results and the corresponding charge and discharge profile of the third cycle at 100 mAh g^{-1}, c) schematic illustration of insertion/extraction of Zn^{2+} in layer structured V_2O_5 host. Reproduced with permission.[37] Copyright 2020, Elsevier. d) Electrochemical in situ/operando Raman mapping and e) waterfall plot of the cathode of Zn/$K_2V_3O_8$ ZIB for the initial cycle. Reproduced with permission.[112] Copyright 2020, American Chemical Society.

cells sealed and thin with a high vacuum system.[44] After Li insertion for 180 s with a constant voltage of –2 V, the width of the V_2O_5 nanoribbon changes from 28 to 31 nm (Figure 12d,e). The ratio of expansion is estimated to be 10% along the (100) direction. Significant volume expansions are mainly observed along the (100) direction because Li ions are mainly stored between the (200) layers. The inset of Figure 12f shows the diffraction pattern of the V_2O_5 nanoribbon after 180 s of Li insertion, which matches the ω-$Li_3V_2O_5$ cubic phase. It is attributed to the large lattice spacing of 5.77 Å between the (200) planes in the Li channel (Figure 12d). The inset of Figure 12f shows the V_2O_5 nanoribbon returns to the origin V_2O_5 with crystal planes (110) and (200) after de-insertion up to 4 V.

AFM is a scanning method for measuring high-resolution surface topology, and this method can measure sample in a liquid environment relatively easily because this analysis does not use electron beams and vacuum system.[39] Like the other analytical cells, a window of in situ/operando AFM cells need to be properly sealed to prevent evaporation of the electrolyte.[44] More detailed design guidelines for AFM cells were reported in refs. [44,118]. Therefore, it allows the monitoring of nanometric grains during electrochemical reactions [=]. Aurbach and Cohen reported unique surface phenomena of V_2O_5 in $LiPF_6$ and $LiClO_4$ for LIBs using in situ/operando AFM.[39] Figure 12g shows topography images of V_2O_5 in a $LiPF_6$/PC solution as electrolyte at three stages: pristine, full insertion, and full de-insertion during the first cycle. After Li full insertion, nanosized round-shaped grains appear on the boundaries of the V_2O_5 particles, with an average diameter of 20 nm. These particles remained after the full de-intercalation, indicating the irreversible reaction. On the other hand, V_2O_5 in a $LiClO_4$/PC solution has no significant change in the micromorphology during Li insertion/de-insertion (Figure 12h). This study demonstrated the impact of the passivation phenomena using images of surface films formations in LIB systems.

6. Summary

V_xO_y is an interesting cathode material for LIBs, NIBs, ZIBs, and MIBs, though it should be cautioned that these electrodes only work with a metal anode, which limits their application. Because of the various compositions, lattice structure, and material morphologies that can be achieved, various V_xO_y materials can be synthesized including V_2O_5, VO_2, $Li_xV_yO_z$, $Na_xV_yO_z$, $Zn_xV_yO_z$, and $Mg_xV_yO_z$. In order to further improve and commercialize these V_xO_y, an in-depth understanding of the science aspect such as structural degradation mechanisms, charge storage mechanisms, and interfacial electrode/electrolyte reactions relating to LIBs, NIBs, ZIBs, and MIBs is crucial. In situ/operando analysis can reveal the real-time structural change, which can be linked directly with the electrochemical properties.

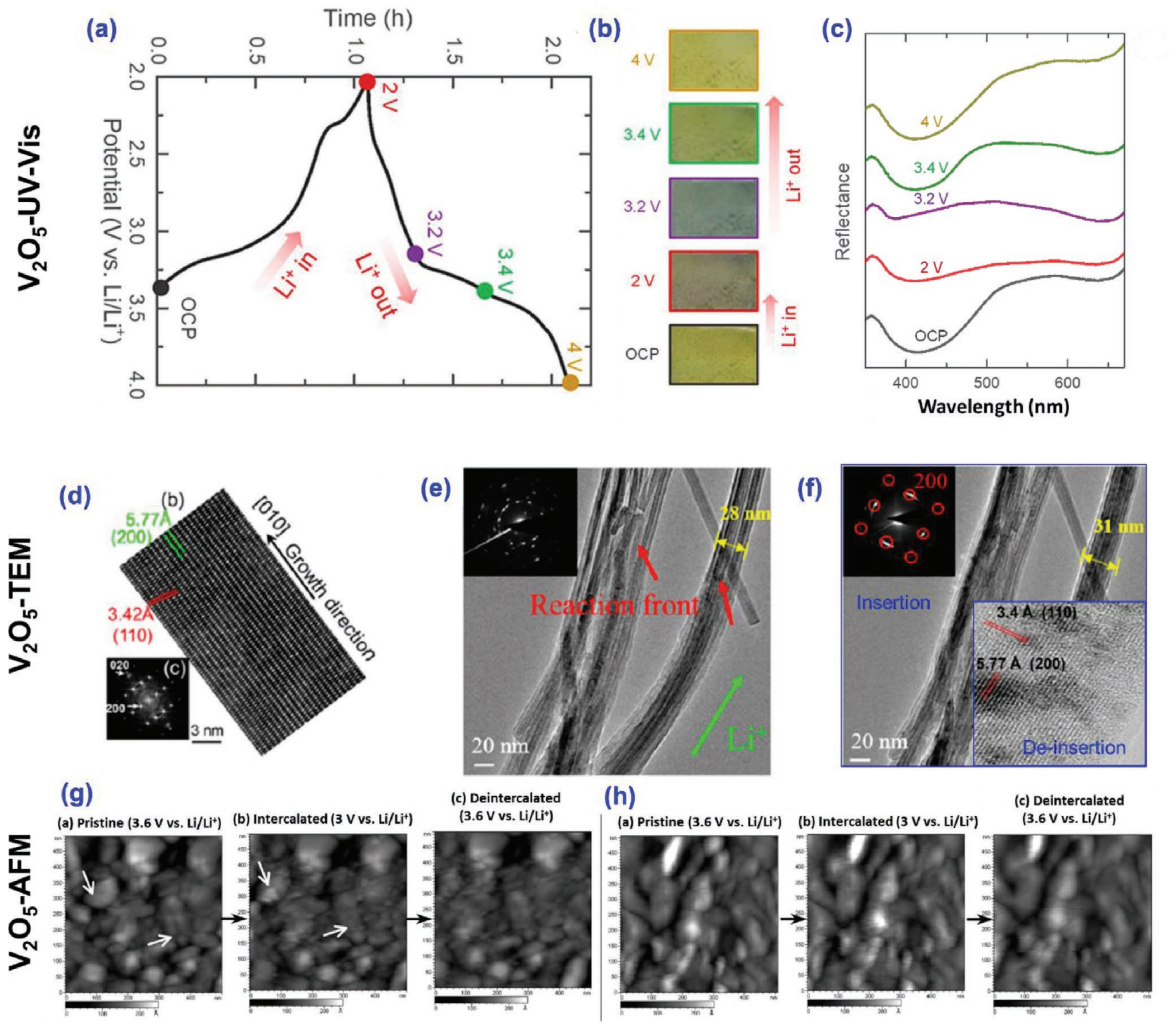

Figure 12. a,b) Initial discharge and charge curve using an optical-cell along with the images showing the change in color as a function of the state of charge of V_2O_5 photocathode of photo-rechargeable LIB. c) The UV-vis absorbance spectra of the photocathode ex situ at the respective states of discharge and charge marked in Figure 12a. Reproduced with permission.[38] Copyright 2021, American Chemical Society. d) High-resolution image (HRTEM) showing the V_2O_5 nanoribbons grown along the [010] direction in situ/operando TEM images of V_2O_5 during e,f) discharging and f, inset) charging. Reproduced with permission.[35] Copyright 2019, American Chemical Society. g) In situ/operando AFM images of V_2O_5 cathodes in g) $LiPF_6$ in propylene carbonate (PC) electrolyte and h) $LiClO_4$ in PC electrolyte for the first cycle. Reproduced with permission.[39] Copyright 2004, Elsevier.

This review paper provides an overview of in situ/operando studies using XRD, XANES, UV-vis, Raman, TEM, and AFM to study V_xO_y cathodes in LIBs, NIBs, ZIBs, and MIBs, although most in situ and operando studies focus on LIBs. The main findings from each operando technique are summarized below and in **Table 2**:

1) In situ/operando XRD traced real-time phase changes, lattice parameter changes, and volume contraction/expansion of V_2O_5, $VO_2(B)$, LiV_3O_8, $Zn_{0.25}V_2O_5$, and $Mg_{0.3}V_2O_5$ electrode materials for LIBs, NIBs, ZIBs, and MIBs. It provided insight into the energy storage mechanisms or structural degradation. This is by far the most frequently reported in situ or operando analysis method applied to V_xO_y cathode materials reported in literature.
2) In situ/operando XAS showed the change in local geometric and electronic structure of materials such as V_2O_5, $VO_2(B)$, and $Mg_{0.3}V_2O_5$, suggesting electronic reversibility of LIBs, ZIBs, and MIBs during cycling.
3) In situ/operando Raman detected variation of the structure at the atomic level such as local disorder, changes in bond lengths and bond angles of a V_2O_5 thin film during ion insertion/de-insertion for LIBs and ZIBs, showing a recovery of the local distortion during ion insertion.

Table 2. Summary of in situ/operando analysis using various vanadium oxides for LIBs, NIBs, ZIBs, and MIBs.

In situ/operando analysis	Change observation	Batteries	Materials
XRD	Phase transformation, lattice parameter, crystallographic structure, and volume contraction/expansion	LIBs	V_2O_5,[18] VO_2(B),[15] LiV_3O_8[27]
		NIBs	$NaVO_2$,[30,76] NaV_6O_{15}[28]
		ZIBs	$Zn_{0.25}V_2O_5{\cdot}nH_2O$,[82] VO_2(B),[14] LiV_3O_8[66]
		MIBs	V_2O_5,[90] $Mg_{0.3}V_2O_5$[24]
XAS	The local geometric and electronic structure	LIBs	V_2O_5,[104,105] VO_2(B)[15]
		ZIBs	V_2O_5,[36] VO_2(B)[108]
		MIBs	V_2O_5,[90] $Mg_{0.3}V_2O_5$[24]
Raman	The structure such as local disorder and changes in bond length and angles at the atomic level	LIBs	V_2O_5[43,109]
		ZIBs	V_2O_5,[37] Zn/$K_2V_3O_8$[112]
Optical characterization and UV-vis	The optical properties	LIBs	V_2O_5[38]
TEM	Morphological atomic lattice	LIBs	V_2O_5[35]
AFM	Surface morphology	LIBs	V_2O_5[39]

4) In situ/operando optical characterization and UV-vis were used to track the change in the bandgap of V_2O_5 electrodes for LIB as a function of the state of charge. By comparison, ZIBs did not show a significant change in bandgap in the voltage range tested so far.
5) In situ/operando TEM provided morphological and atomic lattice information about V_2O_5 nanoribbon for LIBs, showing volume expansion (app 10%) and volume recovery.
6) In situ/operando AFM revealed differences in surface morphology after cycling depending on the type of electrolyte used.

Finally, in situ and operando studies of V_xO_y have not yet been used to study reactions taking place at the electrode/electrolyte interface, material dissolution, or other surface-related degradation mechanisms.

Acknowledgements

The authors acknowledge support from the EPSRC Grant EP/T015179/1.

Conflict of Interest

The authors declare no conflict of interest.

Keywords

in situ/operando analysis, lithium-ion batteries (LIBs), magnesium-ion batteries (MIBs), sodium-ion batteries (NIBs), vanadium oxide, zinc-ion batteries (ZIBs)

Received: June 30, 2021
Revised: August 7, 2021

---

[1] M. Armand, J.-M. Tarascon, *Nature* **2008**, *451*, 652.
[2] D. Larcher, J.-M. Tarascon, *Nat. Chem.* **2015**, *7*, 19.
[3] J. W. Choi, D. Aurbach, *Nat. Rev. Mater.* **2016**, *1*, 16013.
[4] R. Schmuch, R. Wagner, G. Hörpel, T. Placke, M. Winter, *Nat. Energy* **2018**, *3*, 267.
[5] M. Li, T. Liu, X. Bi, Z. Chen, K. Amine, C. Zhong, J. Lu, *Chem. Soc. Rev.* **2020**, *49*, 1688.
[6] T. Liu, Y. Zhang, Z. Jiang, X. Zeng, J. Ji, Z. Li, X. Gao, M. Sun, Z. Lin, M. Ling, *Energy Environ. Sci.* **2019**, *12*, 1512.
[7] B. Dunn, H. Kamath, J.-M. Tarascon, *Science* **2011**, *334*, 928.
[8] G. Fang, J. Zhou, A. Pan, S. Liang, *ACS Energy Lett.* **2018**, *3*, 2480.
[9] J. Xie, Q. Zhang, *Small* **2019**, *15*, 1805061.
[10] M. Liu, B. Su, Y. Tang, X. Jiang, A. Yu, *Adv. Energy Mater.* **2017**, *7*, 1700885.
[11] S. Wang, K. A. Owusu, L. Mai, Y. Ke, Y. Zhou, P. Hu, S. Magdassi, Y. Long, *Appl. Energy* **2018**, *211*, 200.
[12] Y. Yue, H. Liang, *Adv. Energy Mater.* **2017**, *7*, 1602545.
[13] X. Xu, F. Xiong, J. Meng, X. Wang, C. Niu, Q. An, L. Mai, *Adv. Funct. Mater.* **2020**, *30*, 1904398.
[14] J. Ding, Z. Du, L. Gu, B. Li, L. Wang, S. Wang, Y. Gong, S. Yang, *Adv. Mater.* **2018**, *30*, 1800762.
[15] Q. Liu, G. Tan, P. Wang, S. C. Abeyweera, D. Zhang, Y. Rong, Y. A. Wu, J. Lu, C.-J. Sun, Y. Ren, *Nano Energy* **2017**, *36*, 197.
[16] H. Tang, Z. Peng, L. Wu, F. Xiong, C. Pei, Q. An, L. Mai, *Electrochem. Energy Rev.* **2018**, *1*, 169.
[17] P. Nakhanivej, S. K. Park, K. H. Shin, S. Yun, H. S. Park, *J. Power Sources* **2019**, *436*, 226854.
[18] S. K. Park, P. Nakhanivej, K. H. Shin, J. S. Yeon, M. S. Kang, J. B. Lee, H. J. Kim, W. G. Hong, H. S. Park, *J. Alloys Compd.* **2020**, *842*, 155721.
[19] S. K. Park, P. Nakhanivej, J. S. Yeon, K. H. Shin, W. M. Dose, M. De Volder, J. B. Lee, H. J. Kim, H. S. Park, *J. Energy Chem.* **2021**, *55*, 108.
[20] M. S. Kang, S. K. Park, P. Nakhanivej, K. H. Shin, J. S. Yeon, H. S. Park, *J. Alloys Compd.* **2021**, *855*, 157361.
[21] E. Uchaker, Y. Zheng, S. Li, S. Candelaria, S. Hu, G. Cao, *J. Mater. Chem. A* **2014**, *2*, 18208.
[22] G. He, L. Li, A. Manthiram, *J. Mater. Chem. A* **2015**, *3*, 14750.
[23] W. Liu, L. Dong, B. Jiang, Y. Huang, X. Wang, C. Xu, Z. Kang, J. Mou, F. Kang, *Electrochim. Acta* **2019**, *320*, 134565.
[24] Y. Xu, X. Deng, Q. Li, G. Zhang, F. Xiong, S. Tan, Q. Wei, J. Lu, J. Li, Q. An, *Chem* **2019**, *5*, 1194.
[25] Y. Zhang, E. H. Ang, K. N. Dinh, K. Rui, H. Lin, J. Zhu, Q. Yan, *Mater. Chem. Front.* **2021**, *5*, 744.
[26] Q. Wang, J. Xu, W. Zhang, M. Mao, Z. Wei, L. Wang, C. Cui, Y. Zhu, J. Ma, *J. Mater. Chem. A* **2018**, *6*, 8815.
[27] Q. Zhang, A. B. Brady, C. J. Pelliccione, D. C. Bock, A. M. Bruck, J. Li, V. Sarbada, R. Hull, E. A. Stach, K. J. Takeuchi, *Chem. Mater.* **2017**, *29*, 2364.
[28] Y. Dong, J. Xu, M. Chen, Y. Guo, G. Zhou, N. Li, S. Zhou, C.-P. Wong, *Nano Energy* **2020**, *68*, 104357.
[29] M. Yan, L. Zhao, K. Zhao, Q. Wei, Q. An, G. Zhang, X. Wei, W. Ren, L. Mai, *Adv. Funct. Mater.* **2016**, *26*, 6555.

[30] M. Guignard, C. Didier, J. Darriet, P. Bordet, E. Elkaïm, C. Delmas, *Nat. Mater.* **2013**, *12*, 74.

[31] M. A. Bañares, *Catal. Today* **2005**, *100*, 71.

[32] H. Li, S. Guo, H. Zhou, *J. Energy Chem.* **2021**, *59*, 191.

[33] D. Liu, Z. Shadike, R. Lin, K. Qian, H. Li, K. Li, S. Wang, Q. Yu, M. Liu, S. Ganapathy, *Adv. Mater.* **2019**, *31*, 1806620.

[34] X. Ma, W. Luo, M. Yan, L. He, L. Mai, *Nano Energy* **2016**, *24*, 165.

[35] J. Zhu, H. Shen, X. Shi, F. Yang, X. Hu, W. Zhou, H. Yang, M. Gu, *Anal. Chem.* **2019**, *91*, 11055.

[36] H. Zhao, Q. Fu, D. Yang, A. Sarapulova, Q. Pang, Y. Meng, L. Wei, H. Ehrenberg, Y. Wei, C. Wang, *ACS Nano* **2020**, *14*, 11809.

[37] M. S. Javed, H. Lei, Z. Wang, B.-t. Liu, X. Cai, W. Mai, *Nano Energy* **2020**, *70*, 104573.

[38] B. D. Boruah, B. Wen, M. De Volder, *Nano Lett.* **2021**, *21*, 3527.

[39] Y. S. Cohen, D. Aurbach, *Electrochem. Commun.* **2004**, *6*, 536.

[40] C. Heubner, U. Langklotz, C. Lämmel, M. Schneider, A. Michaelis, *Electrochim. Acta* **2020**, *330*, 135160.

[41] A. M. Tripathi, W.-N. Su, B. J. Hwang, *Chem. Soc. Rev.* **2018**, *47*, 736.

[42] T. Hatchard, J. Dahn, *J. Electrochem. Soc.* **2004**, *151*, A838.

[43] G. Zhang, T. Xiong, X. Pan, Y. Zhao, M. Yan, H. Zhang, B. Wu, K. Zhao, L. Mai, *Nano Res.* **2019**, *12*, 905.

[44] P. Harks, F. Mulder, P. Notten, *J. Power Sources* **2015**, *288*, 92.

[45] M. R. Roberts, A. Madsen, C. Nicklin, J. Rawle, M. G. Palmer, J. R. Owen, A. L. Hector, *J. Phys. Chem. C* **2014**, *118*, 6548.

[46] S.-M. Bak, Z. Shadike, R. Lin, X. Yu, X.-Q. Yang, *NPG Asia Mater.* **2018**, *10*, 563.

[47] J. H. Um, S. H. Yu, *Adv. Energy Mater.* **2020**, *11*, 2003004.

[48] M. G. Boebinger, J. A. Lewis, S. E. Sandoval, M. T. McDowell, *ACS Energy Lett.* **2020**, *5*, 335.

[49] F. Yang, X. Feng, Y. S. Liu, L. C. Kao, P. A. Glans, W. Yang, J. Guo, *Energy Environ. Mater.* **2021**, *4*, 139.

[50] K. Palanisamy, J. H. Um, M. Jeong, W.-S. Yoon, *Sci. Rep.* **2016**, *6*, 31275.

[51] B. Kang, G. Ceder, *Nature* **2009**, *458*, 190.

[52] A. Manthiram, *J. Phys. Chem. Lett.* **2011**, *2*, 176.

[53] K. Kang, Y. S. Meng, J. Breger, C. P. Grey, G. Ceder, *Science* **2006**, *311*, 977.

[54] J. Wang, X. Sun, *Energy Environ. Sci.* **2012**, *5*, 5163.

[55] S. Afyon, F. Krumeich, C. Mensing, A. Borgschulte, R. Nesper, *Sci. Rep.* **2014**, *4*, 7113.

[56] C. Delmas, H. Cognac-Auradou, J. Cocciantelli, M. Menetrier, J. Doumerc, *Solid State Ionics* **1994**, *69*, 257.

[57] J. Galy, J. Darriet, A. Casalot, J. Goodenough, *Acta Cryst.* **1964**, *19*, 432.

[58] J. Galy, *J. Solid State Chem.* **1992**, *100*, 229.

[59] J. Cocciantelli, M. Menetrier, C. Delmas, J. Doumerc, M. Pouchard, P. Hagenmuller, *Solid State Ionics* **1992**, *50*, 99.

[60] C. Tsang, A. Manthiram, *J. Electrochem. Soc.* **1997**, *144*, 520.

[61] E. Baudrin, G. Sudant, D. Larcher, B. Dunn, J.-M. Tarascon, *Chem. Mater.* **2006**, *18*, 4369.

[62] C. V. S. Reddy, E. H. WalkerJr., S. Wicker Sr, Q. L. Williams, R. R. Kalluru, *Curr. Appl. Phys.* **2009**, *9*, 1195.

[63] C. Niu, J. Meng, C. Han, K. Zhao, M. Yan, L. Mai, *Nano Lett.* **2014**, *14*, 2873.

[64] C. Nethravathi, B. Viswanath, J. Michael, M. Rajamath, *Carbon* **2012**, *50*, 4839.

[65] S. Liang, Y. Hu, Z. Nie, H. Huang, T. Chen, A. Pan, G. Cao, *Nano Energy* **2015**, *13*, 58.

[66] M. H. Alfaruqi, V. Mathew, J. Song, S. Kim, S. Islam, D. T. Pham, J. Jo, S. Kim, J. P. Baboo, Z. Xiu, *Chem. Mater.* **2017**, *29*, 1684.

[67] C. Wang, M. Wang, Z. He, L. Liu, Y. Huang, *ACS Appl. Energy Mater.* **2020**, *3*, 1742.

[68] Z. Pan, J. Yang, J. Yang, Q. Zhang, H. Zhang, X. Li, Z. Kou, Y. Zhang, H. Chen, C. Yan, *ACS Nano* **2019**, *14*, 842.

[69] N. Liu, X. Wu, Y. Yin, A. Chen, C. Zhao, Z. Guo, L. Fan, N. Zhang, *ACS Appl. Mater. Interfaces* **2020**, *12*, 28199.

[70] S. Liang, T. Chen, A. Pan, D. Liu, Q. Zhu, G. Cao, *ACS Appl. Mater. Interfaces* **2013**, *5*, 11913.

[71] A. Pan, J.-G. Zhang, Z. Nie, G. Cao, B. W. Arey, G. Li, S.-q. Liang, J. Liu, *J. Mater. Chem.* **2010**, *20*, 9193.

[72] Y.-Z. Zheng, H. Ding, E. Uchaker, X. Tao, J.-F. Chen, Q. Zhang, G. Cao, *J. Mater. Chem. A* **2015**, *3*, 1979.

[73] G. Nagaraju, G. T. Chandrappa, *Mater. Res. Bull.* **2012**, *47*, 3216.

[74] Y. Lu, J. Wu, J. Liu, M. Lei, S. Tang, P. Lu, L. Yang, H. Yang, Q. Yang, *ACS Appl. Mater. Interfaces* **2015**, *7*, 17433.

[75] X. Yin, S. Sarkar, S. Shi, Q. A. Huang, H. Zhao, L. Yan, Y. Zhao, J. Zhang, *Adv. Funct. Mater.* **2020**, *30*, 1908445.

[76] C. Didier, M. Guignard, J. Darriet, C. Delmas, *Inorg. Chem.* **2012**, *51*, 11007.

[77] Y. Xu, X. Han, L. Zheng, W. Yan, Y. Xie, *J. Mater. Chem.* **2011**, *21*, 14466.

[78] F. Zhang, M. S. Whittingham, *Electrochem. Commun.* **2000**, *2*, 69.

[79] A. Selvaggi, F. Croce, B. Scrosati, *J. Power Sources* **1990**, *32*, 389.

[80] H. Wang, W. Wang, Y. Ren, K. Huang, S. Liu, *J. Power Sources* **2012**, *199*, 263.

[81] H. Liu, H. Zhou, L. Chen, Z. Tang, W. Yang, *J. Power Sources* **2011**, *196*, 814.

[82] D. Kundu, B. D. Adams, V. Duffort, S. H. Vajargah, L. F. Nazar, *Nat. Energy* **2016**, *1*, 16119.

[83] L. Chen, L. Zhang, X. Zhou, Z. Liu, *ChemSusChem* **2014**, *7*, 2295.

[84] B. Lee, C. S. Yoon, H. R. Lee, K. Y. Chung, B. W. Cho, S. H. Oh, *Sci. Rep.* **2014**, *4*, 6066.

[85] B. D. Boruah, B. Wen, S. Nagane, X. Zhang, S. D. Stranks, A. Boies, M. De Volder, *ACS Energy Lett.* **2020**, *5*, 3132.

[86] L. Chen, Y. Ruan, G. Zhang, Q. Wei, Y. Jiang, T. Xiong, P. He, W. Yang, M. Yan, Q. An, *Chem. Mater.* **2019**, *31*, 699.

[87] D. Chao, C. Zhu, X. Xia, J. Liu, X. Zhang, J. Wang, P. Liang, J. Lin, H. Zhang, Z. X. Shen, *Nano Lett.* **2015**, *15*, 565.

[88] C. Pei, F. Xiong, J. Sheng, Y. Yin, S. Tan, D. Wang, C. Han, Q. An, L. Mai, *ACS Appl. Mater. Interfaces* **2017**, *9*, 17060.

[89] L. Mai, Q. Wei, Q. An, X. Tian, Y. Zhao, X. Xu, L. Xu, L. Chang, Q. Zhang, *Adv. Mater.* **2013**, *25*, 2969.

[90] Q. Fu, A. Sarapulova, V. Trouillet, L. Zhu, F. Fauth, S. Mangold, E. Welter, S. Indris, M. Knapp, S. Dsoke, *J. Am. Chem. Soc.* **2019**, *141*, 2305.

[91] J. Muldoon, C. B. Bucur, T. Gregory, *Chem. Rev.* **2014**, *114*, 11683.

[92] P. Saha, M. K. Datta, O. I. Velikokhatnyi, A. Manivannan, D. Alman, P. N. Kumta, *Prog. Mater. Sci.* **2014**, *66*, 1.

[93] H. D. Yoo, I. Shterenberg, Y. Gofer, G. Gershinsky, N. Pour, D. Aurbach, *Energy Environ. Sci.* **2013**, *6*, 2265.

[94] Y. Sun, L. Zhang, S. Wang, I. Lieberwirth, Y. Yu, C. Chen, *J. Power Sources* **2013**, *228*, 7.

[95] P. E. Tang, J. S. Sakamoto, E. Baudrin, B. Dunn, *J. Non-Cryst. Solids* **2004**, *350*, 67.

[96] R.-H. Kim, J.-S. Kim, H.-J. Kim, W.-S. Chang, D.-W. Han, S.-S. Lee, S.-G. Doo, *J. Mater. Chem. A* **2014**, *2*, 20636.

[97] J. L. Andrews, A. Mukherjee, H. D. Yoo, A. Parija, P. M. Marley, S. Fakra, D. Prendergast, J. Cabana, R. F. Klie, S. Banerjee, *Chem* **2018**, *4*, 564.

[98] H. H. Kristoffersen, H. Metiu, *J. Phys. Chem. C* **2016**, *120*, 3986.

[99] M. Yan, P. He, Y. Chen, S. Wang, Q. Wei, K. Zhao, X. Xu, Q. An, Y. Shuang, Y. Shao, *Adv. Mater.* **2018**, *30*, 1703725.

[100] K. Xu, S. Hu, C. Wu, C. Lin, X. Lu, L. Peng, J. Yang, Y. Xie, *J. Mater. Chem.* **2012**, *22*, 18214.

[101] P. He, G. Zhang, X. Liao, M. Yan, X. Xu, Q. An, J. Liu, L. Mai, *Adv. Energy Mater.* **2018**, *8*, 1702463.

[102] M. A. Lowe, J. Gao, H. D. Abruña, *J. Mater. Chem. A* **2013**, *1*, 2094.

[103] D. Lv, J. Bai, P. Zhang, S. Wu, Y. Li, W. Wen, Z. Jiang, J. Mi, Z. Zhu, Y. Yang, *Chem. Mater.* **2013**, *25*, 2014.

[104] Q. Liu, Z.-F. Li, Y. Liu, H. Zhang, Y. Ren, C.-J. Sun, W. Lu, Y. Zhou, L. Stanciu, E. A. Stach, *Nat. Commun.* **2015**, *6*, 1.
[105] A. Mansour, P. Smith, W. Baker, M. Balasubramanian, J. McBreen, *J. Electrochem. Soc.* **2003**, *150*, A403.
[106] M. Giorgetti, S. Passerini, W. H. Smyrl, S. Mukerjee, X. Yang, J. McBreen, *J. Electrochem. Soc.* **1999**, *146*, 2387.
[107] T. E. Ashton, D. Hevia Borrás, A. Iadecola, K. M. Wiaderek, P. J. Chupas, K. W. Chapman, S. A. Corr, *Acta Crystallogr., Sect. B: Struct. Sci., Cryst. Eng. Mater.* **2015**, *71*, 722.
[108] Q. Pang, H. Zhao, R. Lian, Q. Fu, Y. Wei, A. Sarapulova, J. Sun, C. Wang, G. Chen, H. Ehrenberg, *J. Mater. Chem. A* **2020**, *8*, 9567.
[109] R. Baddour-Hadjean, C. Navone, J. Pereira-Ramos, *Electrochim. Acta* **2009**, *54*, 6674.
[110] R. Baddour-Hadjean, J. Pereira-Ramos, C. Navone, M. Smirnov, *Chem. Mater.* **2008**, *20*, 1916.
[111] T. Gross, L. Giebeler, C. Hess, *Rev. Sci. Instrum.* **2013**, *84*, 073109.
[112] Z. Li, B. Wu, M. Yan, L. He, L. Xu, G. Zhang, T. Xiong, W. Luo, L. Mai, *ACS Appl. Mater. Interfaces* **2020**, *12*, 10420.
[113] K.-Y. Choi, P. Lemmens, V. Gnezdilov, B. C. Sales, M. D. Lumsden, *Phys. Rev. B* **2012**, *85*, 144434.
[114] B. D. Boruah, A. Mathieson, B. Wen, S. Feldmann, W. M. Dose, M. De Volder, *Energy Environ. Sci.* **2020**, *13*, 2414.
[115] Q. Wang, M. Brier, S. Joshi, A. Puntambekar, V. Chakrapani, *Phys. Rev. B* **2016**, *94*, 245305.
[116] G. Wu, K. Du, C. Xia, X. Kun, J. Shen, B. Zhou, J. Wang, *Thin Solid Films* **2005**, *485*, 284.
[117] B. Deka Boruah, A. Mathieson, S. K. Park, X. Zhang, B. Wen, L. Tan, A. Boies, M. De Volder, *Adv. Energy Mater.* **2021**, *11*, 2100115.
[118] D. E. Demirocak, B. Bhushan, *J. Colloid Interface Sci.* **2014**, *423*, 151.

Sul Ki Park received her Ph.D. in Chemical Engineering at the Sungkyunkwan University, South Korea in 2019. Thereafter, she is currently a postdoctoral research associate at the Department of Engineering at the University of Cambridge. Her current research interests focus on energy storage devices, nanostructured materials, and understanding energy storage mechanism.

Wesley M. Dose is a postdoctoral research associate at the University of Cambridge in the Departments of Chemistry and Engineering. Prior to this position, he was a postdoctoral research fellow at Argonne National Laboratory. He received his Ph.D. at the University of Newcastle, Australia. His research interests are in the area of energy storage and electrochemistry, with a focus on understanding the electrode and electrolyte degradation in current- and next-generation batteries.

Buddha Deka Boruah obtained his B.Sc. in Physics from Cotton College, Assam, India and subsequently his M.Sc. in Physics from the Indian Institute of Technology (IIT) Guwahati, India. Thereafter, he received his M.S. in Engineering and Ph.D. from the Indian Institute of Science (IISc), Bangalore, India. He is presently working at the Department of Engineering at the University of Cambridge as a post-doctoral fellow (NIF-Royal Society Fellow). His research interests involve photo-rechargeable energy storage systems, on-chip and planar energy storage devices, UV photodetectors: conventional to self-powered, and advanced hybrid devices: energy conversion and storage.

Michael De Volder performed his Ph.D. research on MEMS actuators at the KU Leuven in Belgium and in part at the Tokyo Institute of Technology in Japan. During his postdoc, he worked on nanotechnology at the Massachusetts Institute of Technology, the University of Michigan, Harvard University, KU Leuven, and Imec. In 2013, he joined the Department of Engineering at the University of Cambridge where he holds a professorship in Advanced Materials Engineering. His work currently focuses on energy storage devices and nanotechnology scale-up.